processes

Review

A Review of Nano and Microscale Heat Transfer: An Experimental and Molecular Dynamics Perspective

Samyabrata Chatterjee [1], Paras [1], Han Hu [2,*] and Monojit Chakraborty [1,*]

[1] Department of Chemical Engineering, Indian Institute of Technology Kharagpur, Kharagpur 721302, India; samyabrata.c@kgpian.iitkgp.ac.in (S.C.); parasdhiman.iitism@kgpian.iitkgp.ac.in (P.)
[2] Department of Mechanical Engineering, University of Arkansas, Fayetteville, AR 72701, USA
* Correspondence: hanhu@uark.edu (H.H.); monojit@che.iitkgp.ac.in (M.C.); Tel.: +91-3222-283932 (M.C.)

Abstract: Significant progress in the development of micro and nanoscale devices has been observed for the past three decades. The thermal transportation in these small-length scales varies significantly, and it is difficult to explain the underlying physics using the pre-existing theoretical formulations. When the bulk dimension of a system is comparable to or smaller than the mean free path (MFP) of the thermal carriers, classical theories, such as Fourier's Law of heat conduction, are unable to accurately explain the system energy dynamics. The phenomena of energy transit and conversion at the micro to nanoscale is an interesting topic of research due to the substantial changes in behavior that are documented when compared to those at the macro size. This review article is broadly divided into two parts. Initially, the recent development in the field of molecular dynamic (MD) simulations is emphasized. Classical MD simulation is such a powerful tool that provides insight into the length scales where the conventional continuum approaches cease to be valid. Several examples of recent developments in the applicability of MD simulations for micro and nanoscale thermal transportation are reviewed. However, there are certain limitations of the MD simulations where the results deviate from experimental validation due to the lack of knowledge of the appropriate force fields. Hence the experimental development of micro and nanoscale thermal transportation processes is briefly reviewed and discussed in the other section of this review article.

Keywords: molecular dynamics; force-fields; thermal transportation; microelectronic devices; liquid thin-film

Citation: Chatterjee, S.; Paras; Hu, H.; Chakraborty, M. A Review of Nano and Microscale Heat Transfer: An Experimental and Molecular Dynamics Perspective. *Processes* **2023**, *11*, 2769. https://doi.org/10.3390/pr11092769

Academic Editor: Ireneusz Zbicinski

Received: 8 August 2023
Revised: 8 September 2023
Accepted: 12 September 2023
Published: 16 September 2023

1. Introduction

According to Moore's Law, the number of transistors that fit into an integrated circuit doubles every second year, indicating the aggressive miniaturization goals of electronic devices over time. These goals are achieved by the improved production of characterized materials with varied length scales. Polymer-nanocomposites [1], multilayer-coating [2], optoelectronic devices [2], microelectronic devices [3], and semiconductor quantum dots [4], are some applications of these characterized materials. However, the major trade-offs while designing these sophisticated and miniaturized devices are the thermal management and energy conversion issues. The control of thermal management requires a complete understanding of the transfer of heat [5] from a system. In micro or nanoscales, the surface-to-volume ratio becomes very high, which makes the classical laws of the heat transfer phenomenon distinctly different [5,6].

Fourier's Law is the most commonly used equation to quantitatively understand the phenomenon of conductive heat transfer. Fourier's Law correlates the relationship among $\dot{Q}$, the heat flux with the thermal conductivity (k), and ∇T, which is the temperature gradient. Various approaches are developed based on this famous relationship, such as the Boltzmann transport equation, atomistic calculations of thermal conductivity [7–9], and many others.

However, several instances have shown that Fourier's Law-based calculations differ significantly when the length scale is reduced to the micro and nano range [6]. One of the widely used methods to identify the violation of Fourier's law is by parameterizing the thermal conductivity [10] of the sample as $\kappa \sim L^{\beta}$, where κ is the thermal conductivity, L is the length of the nanotube, and β is the parameter that identifies the deviation from Fourier's law. $\beta = 0$ identifies the exact correlation with Fourier's law, and when β deviates from zero, certain computational procedures are performed to find the minimum deviation from the experimentally determined value of κ. A detailed analysis of multiwalled carbon nanotubes and boron-nitride nanotubes was conducted by Chang et al. [10]. The thermal conductivity of the superlattice structures [11] and Si nanowires [12] are very low when compared to Fourier's Law. It is well-established that Fourier's Law fails to describe systems when the bulk dimension is comparable or smaller than the mean free path (MFP) of the thermal carriers i.e., phonons and electrons [6,13]. Phonons are mostly important for non-metallic systems where they have a wide range of frequencies and MFPs (1 to 100 nm), and electrons are important for metallic systems. Not only does Fourier's Law require a modification at smaller length scales, but Plank's black body radiation theory also fails to explain the large radiative heat transfer [14,15] when compared to the experimental results that are conducted in a tens of nanometer range of separation. Experimental methods, such as the 3ω method [16], scanning thermal microscopy [17,18], transient thermoreflectance [19,20], the pump-probe technique [21], Raman microscopy [22], photoluminescence [23,24], and thermal conductivity spectroscopy [25] are used to capture the fundamental physics of heat transfer. Even though the experimental devices are getting sophisticated, the lack of accuracy of the measurements remains a major drawback, which leads to the development of several computation methodologies. The Phonon Boltzmann equation [26], Debye approximation of phonon dispersion [27], first principle density functional theory (DFT) calculations [28,29], molecular dynamic (MD) simulations [12,28–32], Atomistic Green's function [33,34], Boltzmann transport equation [34], and Monte Carlo simulations [35] are some of the most popular computational methods used to understand the transportation of heat. Several hybrid methods are being implemented to achieve a higher accuracy of output. The concepts of continuum- and advanced continuum-based models are developed, which were originated by Eringen and his co-workers [36,37] and have found their applicability in developing theories [36–40] of nonlocal elasticity, fluid dynamics, and electromagnetic field theories. A complete mathematical and thermodynamic treatment is performed under two major postulates, namely (a) the energy balance law in the global form and (b) by considering the material body to be only attracted by the neighboring points of the body. The efficiency of these computational methods is increased by using GPU-based computations, high-performance computers, and supercomputers. The computational methods may be very insightful in understanding the thermal transport properties, but it is to be noted that the accurate implementation and the limitations of these methods must be kept in mind to achieve meaningful results.

While designing devices, such as semiconductor lasers and processors of computers, the effective removal of heat becomes the major objective where high thermal conductivity materials are necessary. Single-walled carbon nanotubes (CNTs) and graphene have very high thermal conductivities [41], which are measured using both computational and experimental methods. Nanoparticles when suspended in fluid enhance the thermal conductivity beyond the effective medium [42,43]. This phenomenon has triggered several experimental and computational multiscale studies. Contrary to the high-thermal conductivity devices, low-thermal conductivity materials are equally important for solid-state refrigeration devices. Silicon nanowires, germanium nanowires, WSe_2 crystals, and some superlattices have significantly low thermal conductivity [11,32].

Several of these thermal properties have been estimated both experimentally and computationally. This review is an attempt to put forward the advances in nanoscale heat transportation in both the experimental and computational domains. However, due to the vastness of the computational domain, this article limits the discussion only to

the advances in MD simulation methodologies for micro and nanoscale systems. Some unsolved problems have also been discussed.

2. Molecular Dynamic Simulations

Depending on the length scale and time scale, numerous strategies are implemented to understand the thermal behavior of a system. Figure 1 presents a schematic of the spatiotemporal scale variation and the respective specific strategic tool used. This article is restricted to the domain of micro and nanoscale systems, which range from 10^{-6} to 10^{-9} m. Although other strategic tools are used to understand energy transport in the above-mentioned system length scale, in this article, the discussion is restricted to the development of the MD paradigm only. From Figure 1, it is quite evident that MD covers the overall micro and nanoscale range, and this technique has been studied since 1964 when Rahman found the correlation in the motion of liquid Ar particles and later modified it [31]. MD simulation is an extremely handy tool to study many-body problems at an atomic to molecular scale [30]. MD uses the concepts of statistical mechanics while solving Newton's equation of motion, and the accuracy of the outcomes can be controlled by using realistic many-body inter-atomic potentials. With the recent development in super-fast computing facilities and GPU-based computing, MD simulations have become indispensable in the field of research ranging from biological sciences to material sciences [44–46]. In the next section, a detailed description of the basic principles of MD simulations is provided.

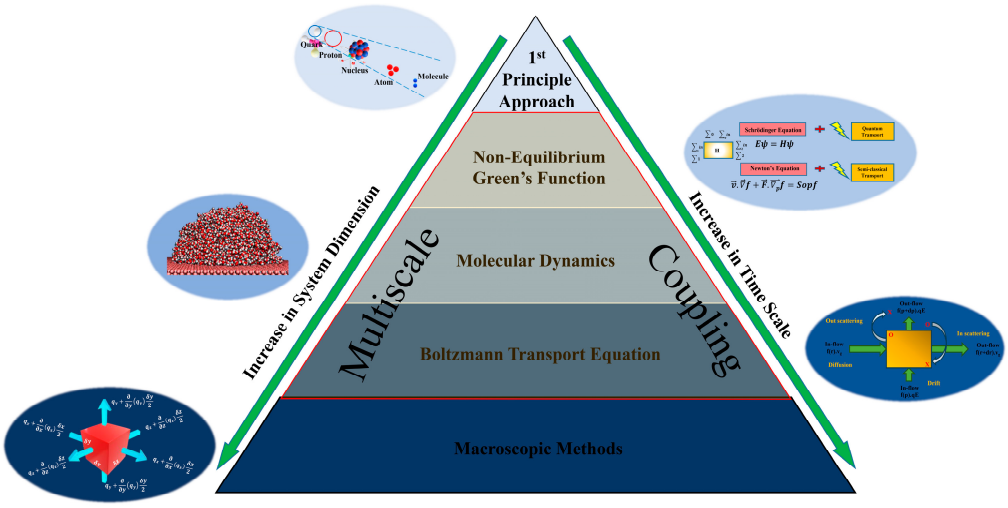

Figure 1. Commonly implemented methodologies with time and length scales.

2.1. Basic Principles of MD

MD simulations originated from the premise that every substance is made up of atoms and molecules, and if the basic parameters of these elementary particles are calculated, some of the macroscopic physical properties, such as temperature, pressure, and volume, can be obtained from the fundamental principles. MD is a bottom-up approach where Newton's second law (Equation (1)) is numerically solved. The law for the atomic scale is written as

$$\vec{F}_i = m_i \frac{d^2 \vec{r}_i}{dt^2} = -\frac{\partial \Phi}{\partial \vec{r}_i} \quad (1)$$

where $\vec{F}_i$ is the force exerted by all the atoms present in a system, m_i is the mass of an atom, $\vec{r}_i$ is the spatial position of a specific atom, Φ is the potential of the system, and t is the time. The displacement of the molecules can be obtained by a double-time integration. If the displacement information within a certain time interval is captured for all the atoms, a piece of detailed information about the atoms can be captured, which can be further analyzed

to obtain certain macroscopic physical properties. However, Newton's second law falls short for complex geometries of the molecules, and a much more generalized version of the original equation is adopted. However, the most important and complicated part of an MD simulation is the choice of the potential of a system, which is derived from ab initio quantum mechanical calculations. Examples of some of the well-established potentials implemented in MD simulations are provided in the next section.

2.2. Example of Some Potential Forms in MD Simulations

The potential of a system is considered to be the sum of effective pair potentials denoted as $\phi(\vec{r}_{ij})$. Mathematically it is expressed as

$$\Phi = \sum_{i} \sum_{j>i} \phi(\vec{r}_{ij}) \tag{2}$$

The term $\vec{r}_{ij}$ represents the distance between molecules i and j. Equation (2) may be a very simplified assumption, but this assumption fails to capture the physics of various complicated geometries or systems at very low temperatures. Hence, the development of several other potential forms became essential. Some of the most commonly used potential forms used in heat transfer research are presented in this section.

2.2.1. Lennard–Jones Potentials

The most commonly used potential is the Lennard–Jones (LJ) 12-6 potential [47] where the molecules are assumed to be symmetric. The LJ potential $\phi_{LJ}(r)$ is defined as follows:

$$\phi_{LJ}(r) = 4\varepsilon_{ij}\left[\left(\frac{\sigma_{ij}}{r_{ij}}\right)^{12} - \left(\frac{\sigma_{ij}}{r_{ij}}\right)^{6}\right] \tag{3}$$

Here, ε_{ij}, and σ_{ij} are the energy and the length scale parameters, respectively. The $\left(\frac{1}{r_{ij}}\right)^{12}$ term represents short-range repulsive interactions, and the $\left(\frac{1}{r_{ij}}\right)^{6}$ term describes the long-range attractive interactions between the atoms/molecules present in the system. Figure 2 depicts the fact that when two atoms come within the diametric distances, they tend to repel each other, whereas atoms present until a certain interatomic distance attract each other, and beyond a certain interatomic distance (2.5 σ), particles do not interact. The minimum potential exists when the interatomic distance is $2^{1/6}\,\sigma$. The LJ 12-6 potential is most commonly used to describe the dynamics of gaseous, especially inert, gases and simple fluidic systems. However, it fails to explain the directional properties of complex many-body systems consisting of directional properties, such as crystal structures and multi-layer graphene.

$$\phi_{LJ}(r) = \begin{cases} 4\varepsilon_{ij}\left[\left(\frac{\sigma_{ij}}{r_{ij}}\right)^{12} - \left(\frac{\sigma_{ij}}{r_{ij}}\right)^{6} - \left(\frac{\sigma_{ij}}{r_{cut}}\right)^{12} - \left(\frac{\sigma_{ij}}{r_{cut}}\right)^{6}\right] & r \le r_{cut} \\ 0 & r > r_{cut} \end{cases} \tag{4}$$

It is to be kept in mind that the major computational calculations are performed while analyzing the potential. This must be performed within a certain cut-off range, or else it may lead to substantial errors considering far-off molecules. Calculations related to pressure or stress must be performed with caution and a proper cut-off distance following Equation (4). However, several other modifications of the LJ potential take account of the continuous decay of the potential with distances, such as the Stoddard and Ford potential [47]. This potential fails to consider the complex geometries or the metallic molecules. One of the most commonly used complex geometric molecules for heat transfer study is liquid water.

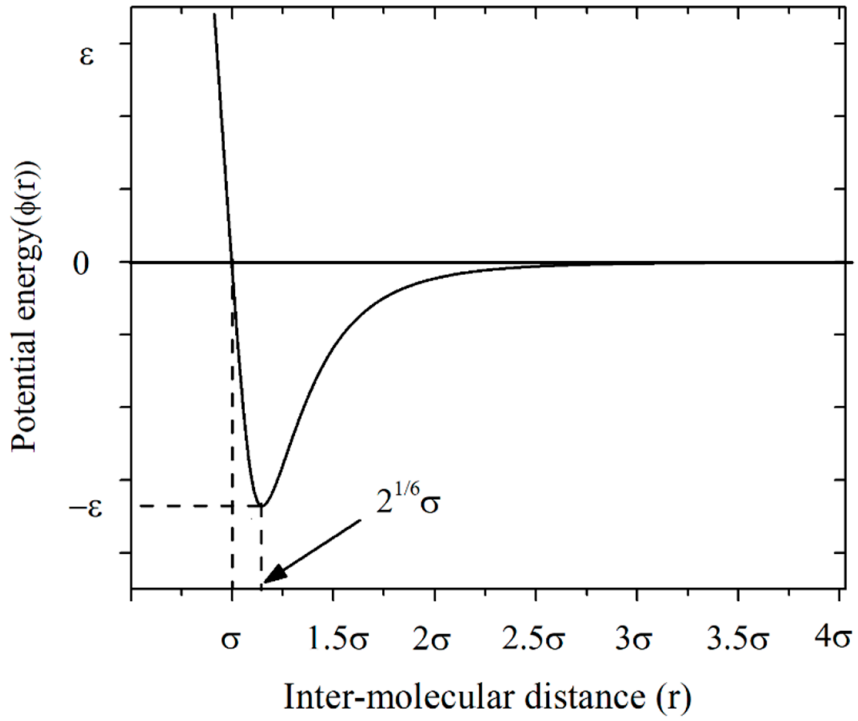

Figure 2. LJ (12-6) potential energy scheme.

2.2.2. Water Models and Potentials

Liquid water is one of the most commonly studied molecules that consist of a complex geometric structure. Due to its applicability as a solvent, water is studied rigorously in computational studies. More than a hundred models exist for water, which indicates the absence of a proper model to define all the properties of real water. It is important to note, that among so many water models, only a few of them capture the temperature dependency of water. SPC, SPC/E, TIP3P, and TIP4P [48] are some of the water models that were parameterized based on experimental data at room temperature conditions. In most of the studies related to heat transfer, TIP4P, and SPC/E are the two rigid water models that are used as they agree well with the surface tension obtained from experiments. A schematic of the water models is presented in Figure 3.

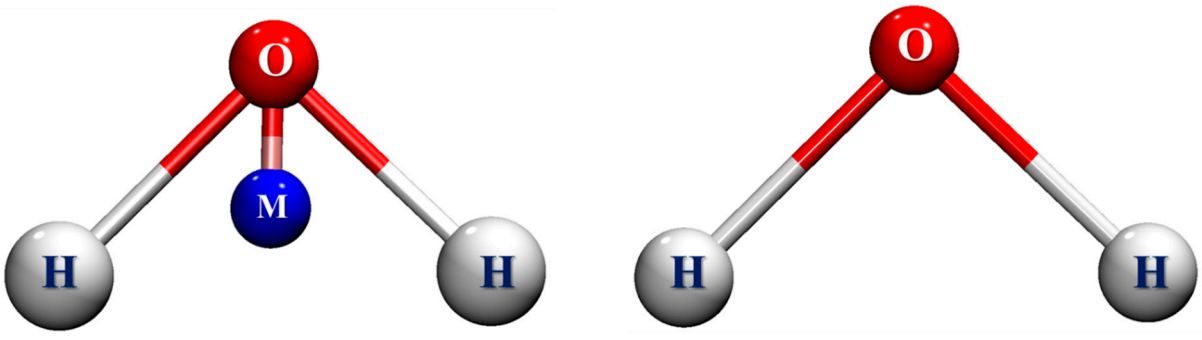

(**a**) (**b**)

Figure 3. Representation of the water models (**a**) TIP4P and (**b**) SPC/E.

(a) TIP4P

TIP4P is a four-site water model, which consists of four interaction points. It adds a dummy atom with a negative charge denoted by M near the oxygen between the two hydrogen molecules as depicted in Figure 3a. The introduction of the dummy charge improves the electrostatic distribution along the water molecule.

(b) SPC/E

The SPC/E model is a three-point model where the three interaction points depict the location of the constituent atoms of water. Each site is considered to be a point charge, and the LJ parameters are assigned to the oxygen atom. An average polarization correction term is added to the potential energy function for the SPC/E model. Figure 3b depicts the SPC/E water model.

Table 1 contains the geometry and parameters for the potential function for TIP4P and SPC/E.

Table 1. Geometry and parameters for potential functions for different water models.

Parameters	TIP4P	SPC/E
r(OH), Å	0.9572	1
<HOH, °	104.52	109.47
A × 10^{-3}, kcal Å^{12}/mol	600	629.4
C, kcal Å^{6}/mol	610	625.5
q(O)	0	−0.8476
q(H)	0.52	0.4238
q(M)	−1.04	0
r(OM), Å	0.15	0

The potential for both of the models is presented as follows:

$$\phi(r) = \sum_{i}^{on\_m} \sum_{j}^{on\_n} \frac{q_i q_j e^2}{r_{ij}} + \frac{A}{r^{12}{}_{OO}} - \frac{C}{r^{6}{}_{OO}} \quad (5)$$

Here, A and C are the LJ parameters, q_i and q_j are the charges of the interacting molecules, e is the electron charge, and r_{OO} is the distance between two oxygen atoms. For the SPC/E potential [48,49], an additional average potential correction term is used and is given as follows:

$$\phi_{pol}(r) = \frac{1}{2}\sum_i \frac{(\mu - \mu^0)^2}{\alpha_i} \quad (6)$$

where μ is the dipole moment of the polarized water molecule, μ^0 is the dipole moment of an isolated water molecule, and α_i is an isotropic polarizability constant. It is to be noted that several other water models are used for different types of molecular systems, which are described in detail elsewhere [48].

2.2.3. Other Commonly Used Many-Body Potentials

Covalently bonded chemical structures are such structures where the pair potential approximation fails to provide accurate results. In such scenarios, many-body potentials, such as Stillinger and Weber [50] potential, Tersoff potential [51], EAM potential [52,53], and MEAM potential [54], are implemented. Due to its wide applicability and non-reactive properties, silicon is one of the most commonly studied chemical compounds using MDs in micro and nanoscale heat transfer domains. Silicon is a covalently bonded molecule, and hence, two- and three-body terms are introduced by Stillinger and Weber to study the diamond structure of silicon. Later, Tersoff potential is introduced to study carbon, germanium, and various compounds of these atoms along with the silicon. The Tersoff potential allows the covalent bonds to form and dissociate, which are captured by the bond order parameters [51]. The bond order parameter depends locally on the chemical environment, which decides the strength of the bond. Due to this parameter, the Tersoff

potential can identify the mixed hybridization of the materials. The Tersoff potential [51] is defined as follows:

$$\phi_{Tersoff} = \frac{1}{2}\sum_{i}\sum_{i\neq j} f_c(r_{ij})[f_R(r_{ij}) + b_{ij} f_A(r_{ij})] \quad (7)$$

where $f_c(r_{ij})$ is the simple decaying function term, $f_R(r_{ij})$ is the two-body-repulsive term, $f_A(r_{ij})$ is the three-body attraction term, and b_{ij} is the attractive force modification term.

Metal surfaces and structures are very common in micro and nanoscale heat transfer studies, and hence, a discussion regarding the potentials used to conduct MD simulations is briefly discussed herein. Metals have unfulfilled valence shells, which is why the non-interacting bond strength approximation fails and the requirement of a new potential arises. The embedded atom method (EAM) is the most commonly used semi-empirical and many-atom potential. The potential is defined as the sum of the function of separation between an atom and its neighbors. The cumulant of effective embedding density is used as a correction term for the pairwise interactions and is considered a function of the combined effective neighbor density. The EAM potential function is represented as follows:

$$\phi_{i,EAM} = F_\alpha\left(\sum_{j\neq i}\rho_\beta(r_{ij})\right) + \frac{1}{2}\sum_{j\neq i}\phi_{\alpha\beta}(r_{ij}) \quad (8)$$

Here, F_α is the embedding function, $\phi_{\alpha\beta}$ is the pairwise potential function, and ρ_β is the electron charge density of the jth atom of type β at the location of the ith atom.

The EAM model may be a powerful tool for bulk metals, but a much more generalized form is the modified embedded atom method (MEAM). EAM potential may be inadequate near surfaces and defects, and hence, an additional electron density term is incorporated into the MEAM potential calculation, which is presented as

$$\phi_{MEAM} = \sum\left(F_i(\bar{\rho}_i) + \frac{1}{2}\sum_{i\neq j}\phi_{ij}(r_{ij})\right) \quad (9)$$

Here, F_i is the embedding function, which is dependent on the atomic electron density ρ_i, and ϕ_{ij} is the pairwise potential function.

This section depicts the importance of proper choice potential in designing a nano/microscale heat transfer MD simulation and keeping the model as realistic as possible. However, a realistic MD simulation is conducted based on the correct choice of parameters, such as proper boundary conditions, ensembles, temperature and pressure control, and most importantly, the time integrator.

A molecular understanding has become more and more important owing to the recent adaptation of the bottom-up approach. Phase change heat transfer, wetting, nucleation, evaporation, condensation, bubble formation, thin film formation, and so on, have been studied using MD simulations to understand the physics at smaller length scales and, due to their applicability, in various micro and nano-technologies. The next section depicts the application of MD simulations in various micro and nano-technologies.

3. Application of Molecular Dynamic Simulations in Micro and Nanoscale Heat Transfer

This section of the article describes the importance and impact of MD simulations by portraying several applications in the field of micro and nanoscale heat transfer. There are two broad categories in which MD simulations have made noteworthy advances, namely (a) energy transport during the phase change processes at the interfaces and (b) heat conduction. The phase change scenarios occur at the liquid–vapor interface, solid–liquid–vapor interphases, and during the nucleation, coalescence, and in many other similar conditions. However, this review is limited by not considering the phonon transport processes in

conduction heat transfer applications, as the phonon transfer requires a separate treatment compared to the conventional experimental and theoretical approaches.

3.1. Liquid–Vapor Interface

3.1.1. Liquid Droplet at the Vapor Interface and Surface Tension

A typical liquid–vapor interface setup for an MD simulation consists of a liquid wedge in between one or two vapor regions. If the liquid region is thick enough, the bulk properties of the system can be calculated from the central region by considering the time-averaged values of density, pressure tensor, and surface tension. It is customary to validate the surface tension to check the rationality of the potential function model being used. One of the most common and accurate methods to calculate surface tension [55,56] (γ_{LG}) for LJ-fluids and water is by

$$\gamma_{LG} = \int_{z_L}^{z_G} [P_N(z) - P_T(z)]dz \quad (10)$$

Here, $P_N(z)$ and $P_T(z)$ represent the normal and tangential components of the pressure tensor, which is equal to the thermodynamic pressure at the bulk vapor position at z_G and the bulk liquid position at z_L. To maintain the equilibrium and consider the system to be in equilibrium $P_N(z)$, along the interface must be constant. Equation (10) is widely used to calculate γ_{LG} as it reduces the numerical fluctuations and takes care of the non-uniform density distribution at the interface.

There are several ways to calculate coexisting liquid and vapor densities. Some of the examples include MD [55] simulations, the Gibbs simulation technique in the Monte Carlo method [57], the chemical potential and pressure function, and direct methods [55]. However, some of these methods cannot be used directly or are computationally too expensive to calculate interfacial properties, such as surface tension. But Holcomb [58] confirmed that the direct methods generate high-accuracy surface tension data. Alejandre et al. [56] later confirmed that the SPC/E water model can predict surface tension at varying temperatures with high accuracy. Their study reported the variation in surface tension for temperatures from 316 K to 573 K. The experimental and theoretical findings are in reasonable agreement for temperatures lower than 573 K, but they tend to deviate for higher temperature conditions. They also concluded that the direct method can be used at the triple point. However, smaller systems do not have a proper central region, so the above-mentioned methods fail and statistical mechanical calculations are adopted. Zakharov et al. [59] also described the importance of the choice of the proper cluster size of the water molecules as it directly affects the surface tension. According to their paper, the orientation of the water molecules at the interface highly depends on the water model implemented, which indirectly affects the surface tension.

3.1.2. Mass Transfer at the Liquid–Vapor Interface

Mass and heat transfer processes are highly important for fluid separation processes, absorption, distillation, and various chemical engineering unit operations. A recent study by Schaefer et al. [60] performed a dual control volume (DVC) based non-equilibrium MD simulation (NEMD) to understand the concentration gradient-based interfacial mass transfer under different temperature conditions. A detailed structure of the system is depicted in Figure 4a. Figure 4b indicates that component 2 is highly sensitive to variation in temperature and is maximum for mixture B. Due to the smaller solubility of component 2 in the liquid phase, it is less sensitive to temperature. However, it validates the concept of enrichment, which is lower at higher temperatures and vice versa.

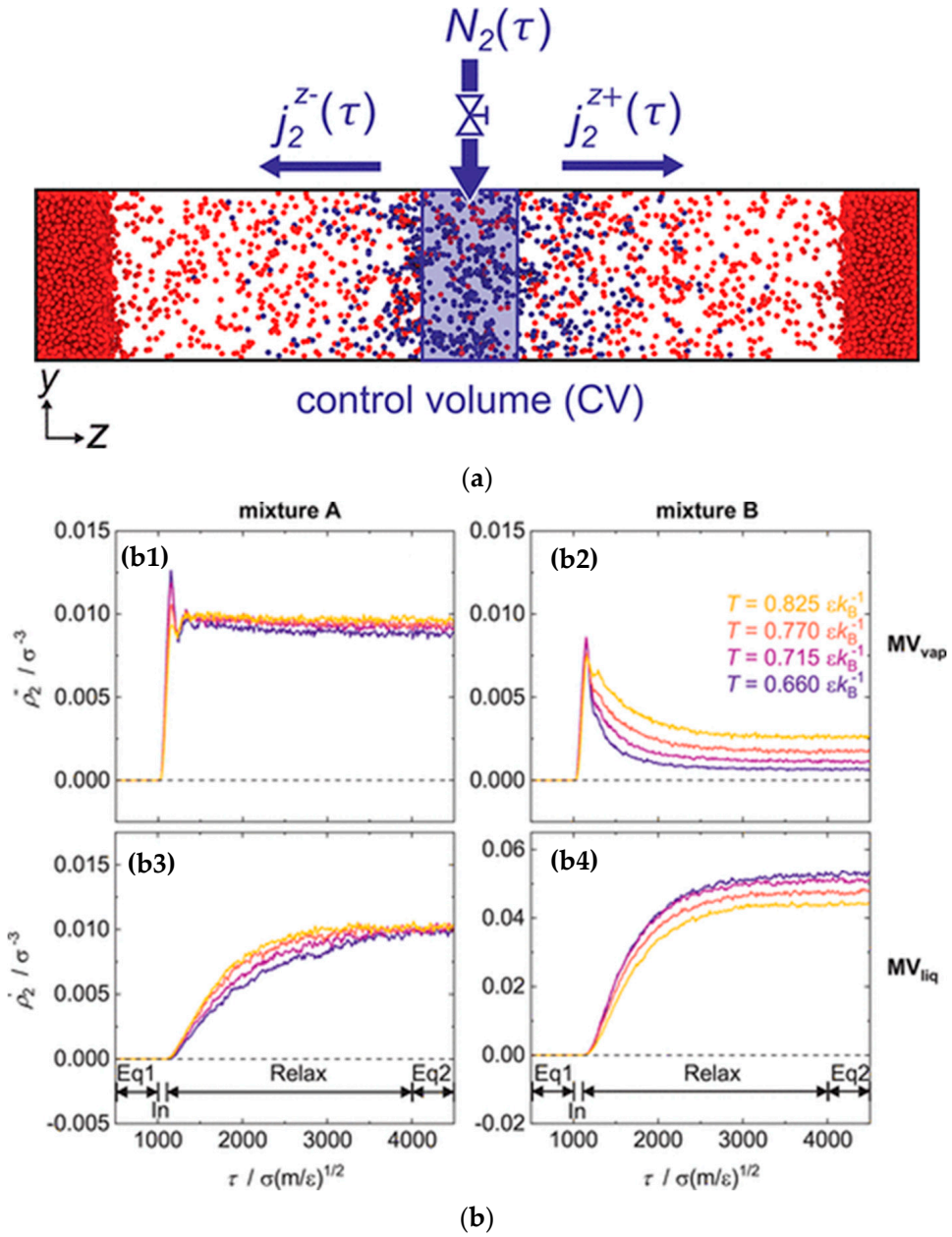

Figure 4. NEMD simulation setup and the simulation outcome. (**a**) Non-equilibrium MD set-up, and (**b**) variation in the density for component 2 under different thermal conditions [60]. Reprinted with permission from Schaefer et al. [60].

3.1.3. Evaporation at the Liquid–Vapor Interface

Evaporation is one of the most important interfacial phenomena and has huge applications in engines, thermal management, and micro-cooling technology [61]. The initial studies of evaporation were conducted by Long et al. [62] for liquid argon droplets in subcritical and supercritical surroundings. The outcomes were in good agreement with experimental studies. Subcritical evaporation of a nanodroplet was later conducted by Walther et al. [63] The simulation was conducted at 300 K and 3 MPa using an adaptive tree data structure and neighbor lists for a larger number of molecules. The evaporation coefficient data were in impressive agreement with theoretical predictions. Yang et al. [64] performed MD simulations with the TIP4P water model and vapor as presented in Figure 5a.

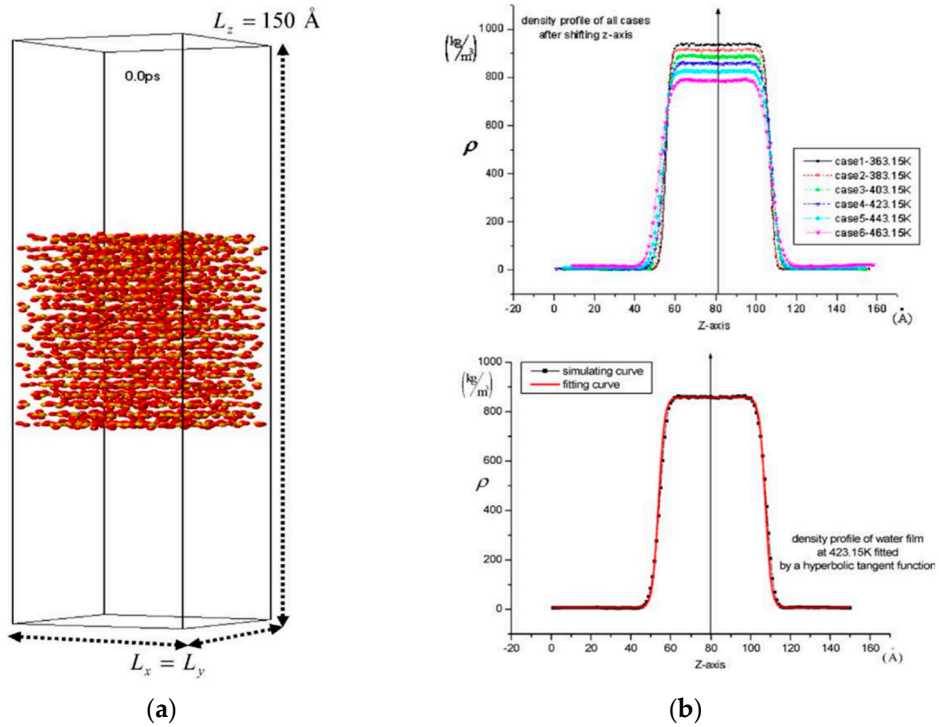

(**a**) (**b**)

Figure 5. Air–water interface simulations and density profile analysis. (**a**) Initial set-up of the simulation, and (**b**) demarcation of the three regions from the density profile plot. Reprinted with permissions from Yang et al. [64].

Density profiles under varying thermal conditions have been studied, as depicted in Figure 5b, where the three regions, the (a) liquid layer, (b) transition layer, and (c) vapor region, are demarcated distinctly after the equilibrium was attained. The temperature variation for different regimes was observed, and the mean temperature was lower in the liquid layer and was maximum at the interface. The evaporation coefficients were in good agreement with various experimental and theoretical studies. However, the previously conducted studies were performed using equilibrium MD techniques, but in the recent past, with the development of newer models, non-equilibrium MD (NEMD) has been adopted. Heat transfer is a non-equilibrium process, and the incorporation of variation in the spatial thermal gradient has made NEMD simulations more realistic. Moreover, Fourier's law can be only examined through a non-equilibrium heat conduction calculation for microscopic systems [65]. In the case of a two-phase evaporating system [66], the vapor phase is designated at a certain distance from the interface, which is known as the Euler regime, and particles ejected from the interface propagate through the Knudsen layers towards the Euler regime. The temperature variation is observed in the Knudsen layer, and the particles are considered to follow the Maxwell velocity distribution in this regime. Persad and Ward [65] concluded that the Hertz–Knudsen formulation is incomplete as it showed huge variation in data ranges for evaporation experiments with water and ethanol. Later, Frezzotti and Barbante [65] chose to vary the kinetic boundary conditions along with larger vapor regions, which mimicked the Euler regime with very high accuracy. Heinen et al. [66] conducted an NEMD study to understand the evaporation across a planar surface. Interestingly a new and much better algorithm was introduced to yield high-accuracy density, temperature, and force profiles. They modified the pre-existing particle insertion method, which is a common practice to maintain mass conservation in MD simulations. However, this method gives rise to reducing the potential energy threshold, which leads to local instability. The drawback was resolved through the introduction of liquid and vapor compartments in conjunction with control volumes along with specifying the thermodynamic properties at the system boundaries.

3.1.4. Behavior of Long-Chain Organic Molecules at the Liquid–Vapor Interface

Long-chain hydrocarbons are of huge interest owing to their applicability as surfactants and in various applications in petrochemical industries, such as enhanced oil recovery (EOR), Fischer–Tropsch synthesis, carbon capture, and many others. He et al. [67] performed NEMD simulations on n-heptane/ethanol mixtures under different thermal conditions. In subcritical conditions, the enhancement of the ethanol concentration increases the evaporation rate. This is due to the decrease in vapor pressure and enhanced thermal conductivity. However, when the supercritical condition is considered preferential, the diffusion of ethanol is observed. Interfacial thickness and interfacial resistances are studied in detail as they have a huge impact on evaporation characteristics. Ambient pressure has a huge impact on thermal conductivity, which decreases with pressure under transcritical conditions.

Yang et al. [68] recently investigated the liquid–vapor interfacial behavior for straight and branched-chain alkanes and alcohols using MDs. The structures of the chosen molecules are depicted in Figure 6a. OPLS-AA, TraPPE-UA, and L-OPLS models were considered. The force field data were calibrated to experimental data for the molecules used under the 323.15 K to 573.15 K temperature range. For lower temperatures, all the force fields produced comparable self-diffusion coefficients, liquid densities, and surface tensions. However, the TraPPE-UA force field was able to accurately predict the solvation structures and reproduce the most promising results, considering the overall range of temperatures. Liquid density profiles under different temperature conditions were produced as presented in Figure 6b. The results concluded that elongation of the molecules occurs due to strong polar interactions, and hence, they have higher energy to remain in the liquid phase.

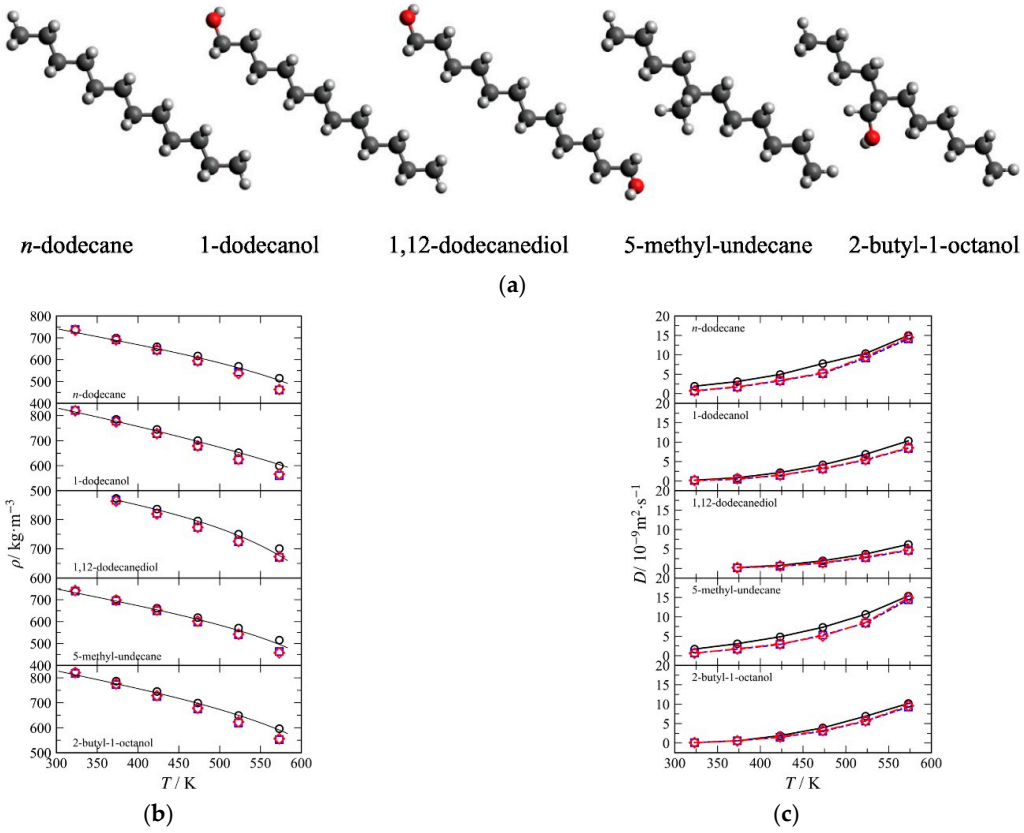

Figure 6. Long chain organic molecules at the liquid–vapor interface and subsequent results on thermal alteration. (**a**) Chosen molecules for the simulation, (**b**) liquid density data for different temperatures, and (**c**) the self-diffusion coefficient as a function of temperature. Reprinted with permissions from Yang et al. [68].

Longer chain molecules tend to display directional behavior at the interface. Also, a detailed calculation of the self-diffusion coefficient was conducted using the Einstein relation [68] given as

$$D = \frac{1}{6}\lim_{t\to\infty}\frac{d}{dt}\left\langle \frac{1}{N}\sum_{i=1}^{N}|r_i(t) - r_i(0)|^2 \right\rangle \quad (11)$$

Here, D is the self-diffusion coefficient, N is the number of particles, and $r_i(t)$ represents the variation in the displacement of the ith particle. The trend in the self-diffusion curve increases with temperature, as presented in Figure 6c. The application of long-chain alcohols can be observed for scenarios of surfactant behavior at the vapor–liquid interface. Daiguji [69] simulated long-chain alcohols using an OPLS force field in the presence of an SPC/E water model. Instability at the interface was observed for n-heptanol at a certain concentration. For lower alcohol concentrations, the interface was stable owing to the hydrophilic and hydrophobic interactions. Increasing concentrations of hydrophilic alcohol molecules lead to an unstable interface.

3.1.5. Effects of a Pressure-Varying Field on Vaporization

Periodic pressure oscillation is induced by combustion instability during the launch of a rocket. The instability of combustion may lead to increased vibration and heat loads. Unstable combustion is a complicated combination of evaporation, atomization, and combustion. However, several studies have suggested that the nature of droplet evaporation is one of the major reasons for dynamic pressure behavior. Hence, it became essential to understand the droplet evaporation process in the presence of pressure oscillation. One of the first studies was conducted by Arcidiacono et al. [70], where argon was used as a droplet and the droplet was imposed in a velocity field to make it oscillate freely. The oscillation and damping constant frequency was within 20% of macroscopic theories. Sheu et al. [71] conducted numerical studies to understand the effects of evaporation under the adiabatic compression process. Their study suggested that evaporation was higher under constant pressure conditions but it increased drastically under compression. Liu et al. [72] used MD simulations to simulate the evaporation of an SPC/E-modeled water droplet. The simulation environment was oscillated using a standing wave acoustic field. The acoustic field was depicted as follows:

$$m_i\frac{d^2r_i}{dt^2} = F_i + F_e = \sum_{j=1,j\neq i}^{N} f_{ij} + F_e \quad (12)$$

Here, F_i is the total force exerted on the ith molecule by the other molecules, and F_e is the force of periodic oscillation on the particles in a standing wave acoustic field. F_e is given as

$$F_e = A_0\cos(wt)\sin(\beta x) \quad (13)$$

where $w = \frac{n\pi v}{l}$ and $\beta = \frac{w}{v_c}$, A_0 is the amplitude, n is the number of standing waves, ω is the frequency, and v_c is the speed of the acoustic wave. The surrounding of the water molecule was filled with nitrogen molecules. The temperature for the water molecule and nitrogen molecule were set to 298 K and 1000 K, respectively. The oscillation frequency, pressure amplitude, and temperature have significant effects on the evaporation rate. It was observed that a lower amplitude indicated a higher droplet lifetime, which occurred due to a decrease in the droplet temperature. Similarly, at higher frequencies, the evaporation increases rapidly, but the oscillation tends to diminish beyond a specific frequency.

3.2. Solid–Liquid–Vapor Interface

3.2.1. Liquid Droplets on Solid Surfaces

Solid–liquid–vapor interactions are very important for multiphase heat transfer. Liquid wettability is one of the most important factors that govern heat transfer during boiling, capillary liquid film evaporation, dropwise condensation, and thin-film evaporation. The

phenomena of droplet spreading are associated with the wetting qualities of any substrate. Wetting properties, such as the contact angle and contact diameter, are calculated by obtaining the data from MD simulations.

Figure 7a,b depicts the water droplet on a Cu (1 0 0) surface [73] and the density plot to calculate the water droplet interface, which is further analyzed to calculate the contact angle and contact diameter using traditional curve-fitting methodologies. The droplet tends to modify its shape until it reaches an equilibrium shape. Previously, the concept of a "mono-layer liquid Film" was very popular, but several theories on the three-phase contact-line were developed based on the movement of the wetting line. The detailed theories connecting the microscopic and macroscopic explanation of the wetting phenomenon were explained by Dussan [74], Banavar, and Koplik [75]. In the most recent theories, it is considered that even though multiple resistances are encountered throughout the movement of the wetting line, the contact line frictional force (CLF) is the dominating one [76]. According to Blake [77], statistical analysis of molecules present in the three-phase zone (TPZ) could be used to identify the displacement of the contact line. The three-phase contact line (TPCL) friction force is the force acting in the TPZ. The TPCL friction force is molecular in nature, and MD research is considered an obvious choice for understanding the impacts of crystal planes on analogous wetting parameters at an atomic level. Molecular Kinetic Theory [78,79] (MKT) is a model that is commonly used in conjunction with AMD simulations for the improved understanding of water-spreading dynamics on hydrophobic surfaces [77], droplet motion on gradient surfaces [80], contact line movement in electrowetting [81,82], different crystal planes [73], and various other similar studies.

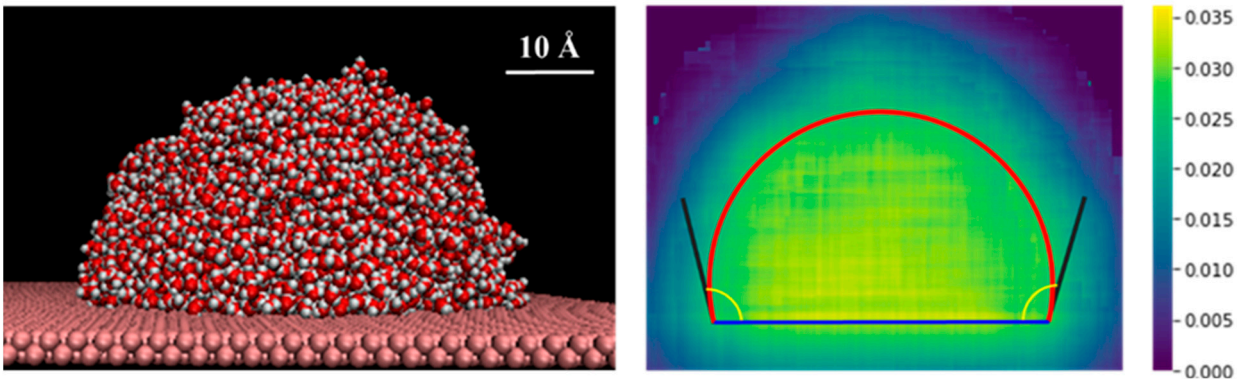

(**a**) (**b**)

Figure 7. Schematic representation of molecular simulation of a sessile droplet for the estimation of the contact angle at the solid–liquid–vapor interface. (**a**) Equilibrated water droplet, and (**b**) analysis of the contact angle using the density profile of the droplet. Reprinted with permissions from Chatterjee et al. [73].

3.2.2. Impact of Interaction Parameter and Molecular Kinetic Theory at the Three-Phase Contact Line

In all the above-mentioned applications, the interaction parameter plays the most important role. A detailed analysis of the wetting properties, such as the contact angle and contact radius, was conducted by Chakraborty et al. [80], where the SPC water model was used. Figure 8a shows that the contact angle rapidly decreases and the contact radius increases with increasing interaction parameters between the solid and the water molecules. Figure 8b indicates that the velocity of the droplet for a particular interaction parameter is temperature-dependent. It shows a steady increase and then a sharp decrease after reaching the maxima, which is in perfect sync with reported experimental observations [76]. The variation in velocity directly affects the contact angle and contact diameter, which, on the other hand, indicates the variation in contact line frictional forces. A detailed MKT analysis was performed to understand the variation in the contact line friction coefficient

with temperature. Figure 8c indicates the highly correlated theoretical and MD predictions. However, it is to be noted that the contact line friction force coefficient cannot be directly correlated with experimental observations as the length scale of an actual droplet and droplet used in MD simulations differ by multiple orders of magnitude.

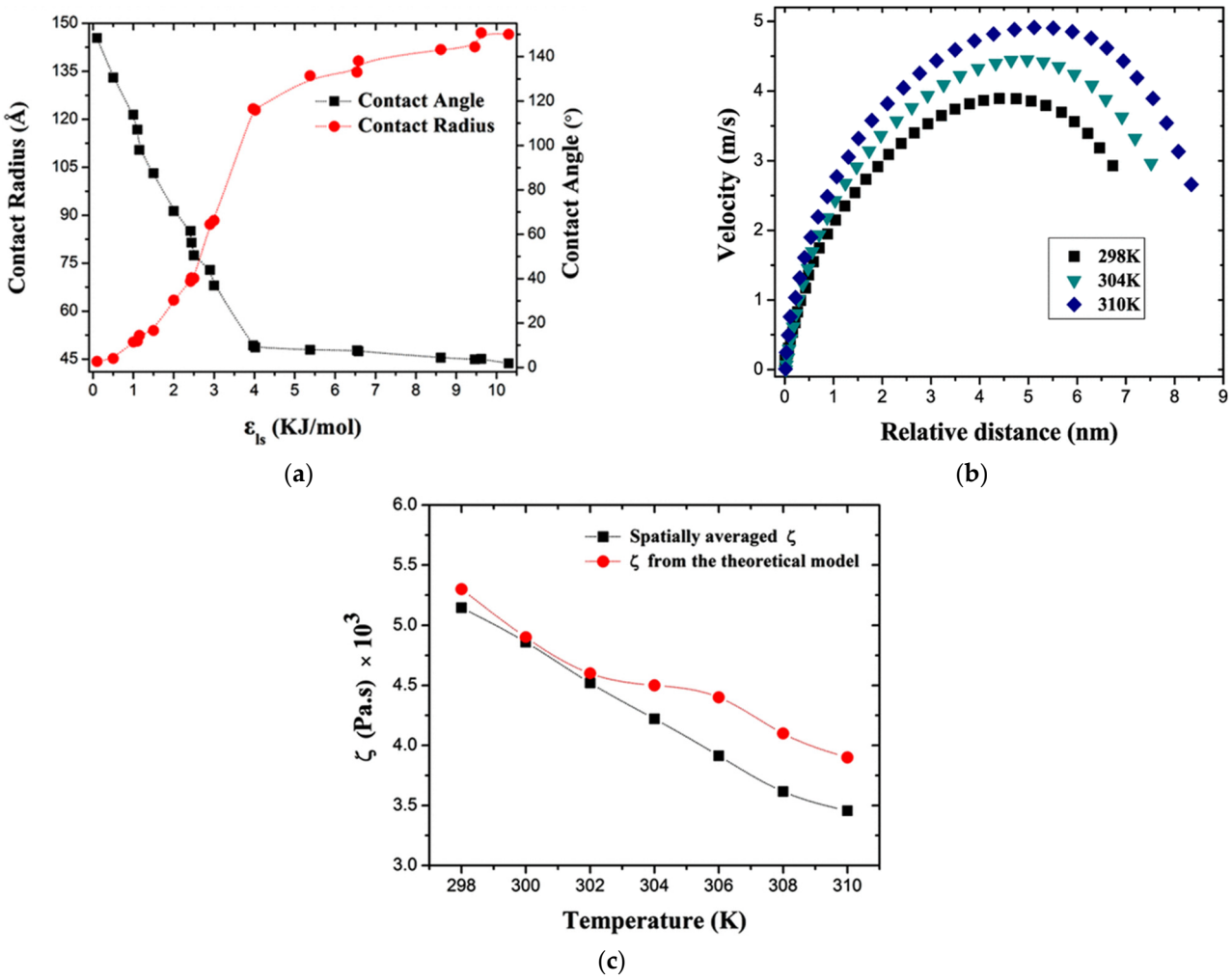

Figure 8. Molecular investigation of the various parameters during a nanoscale droplet spreading and movement. (**a**) Variation of the interaction parameter and contact angle and contact radius, (**b**) analysis of the velocity of the droplet at different temperatures, and (**c**) analysis of the contact line friction at different temperatures. Reprinted with permissions from Chakraborty et al. [80].

3.2.3. Liquid Droplet–Carbon Nanotube Interface

Carbon nanotubes (CNTs) were first synthesized in 1991 and are still being investigated owing to their amazing mechanical, electrical, and thermal properties. CNTs are widely used in heat transfer enhancement, nano actuators, water filtration, tips of atomic force microscopy, and many others. Walther et al. [83–85] performed the first AMD simulations with CNT and SPC water models. They investigated CNT in a water environment and the behavior of water droplets inside a CNT. Their study suggested that water does not wet CNT in a water environment. The water droplets inside the CNT align themselves in parallel to the CNT surface keeping a few angstrom gaps. However, the results were far off from the experimental results mostly due to the purity of water selected for either study. Casto et al. [86] used AMD simulations to understand the effect of mass transfer and heat transfer mechanisms as a function of the CNT surface. LJ interaction parameters were varied between the interface and the water molecules to understand the water-filling mechanism inside the CNT. A phenomenological parameter β was introduced to

correlate the wettability and the diameter of the CNT. The wettability of a surface plays a huge role in the thermal conductivity at the interface. The parameter calculated to understand the interfacial thermal flow hindrance is known as the thermal boundary resistance (TBR) or Kapitza resistance. A detailed analysis was conducted on the TBR while varying the interaction parameters. The study suggests that hydrophilic conditions enhance heat transfer due to more structured solids, like water. Similar studies have been conducted by Jabbari et al. [87] using NEMD simulations depicting analogous results, and a proper correlation was derived between the Kapitza resistance and the interaction between CNT/water and graphene/water nano-fluids.

It is well established in the literature that the introduction of graphene in CNT-based nanocomposite phase-change materials (NPCMs) enhances thermal conductivity. Du et al. [88] used AMD simulations to understand the intrinsic mechanism to enhance the thermal properties of NPCMs. The distribution of the phase-change molecules (PCMs) near the CNT wall plays a major role along with low PCM, which enhances the mobility of the molecules. However, the results show that over-filled PCM reduces the thermal conductivity and proper frame stacking of CNT enhances the thermal conductivity of the system. These NPCM-based systems have huge implications in the field of thermal energy storage devices, which is considered as one of the many alternate energy sources. However, along with MD simulations, several continuum-based theories have been developed to explain the thermoelastic responses of double-walled CNTs. These models are developed based on the nonlocal elasticity theory of Gurtin–Murdoch [89,90] and Eringen [36,37]. Kiani [39,40,91–93] later modified the theories for various micro and nanoscale systems. Detailed information on continuum-based models can be found elsewhere [39,40,91–95]. Pakzad et al. [96] performed atomistic MD simulations to address the anisotropic treatment of Si nanowire surface properties. The multiscale nano-mechanical model implemented is based on the extended Young–Laplace linear surface elasticity model [97] within the Euler–Bernoulli beam formulation. However, the discussion of this paper is limited to the realm of MD simulations. Interested readers can go through detailed discussion on such multiscale modeling studies elsewhere [96,98–102].

3.2.4. Bubble Dynamics at the Solid–Liquid–Vapor Interface

Owing to the ever-expanding field of micro-electronic fabrication, studies on bubble dynamics have received significant interest from the research community. In microchannels, studies suggest that for single-phase flow, surface wettability plays a huge role in the heat transfer characteristics of the system. However, in micro-heat exchangers that consider phase-changing working media, bubble formation arises under certain circumstances. Classical theories portray the high superheating requirement to form a nano-bubble. Several MD simulation-based studies have been conducted by Kinjo and Matsumoto [103] and Maruyama and Kimura [104], where the classical nucleation theory was validated. Later Kinjo et al. [103] worked on the effects of different types of surfaces, such as hydrophobic and hydrophilic. Still, the origin of bubbles near the surfaces was not clear. Nagayama et al. [105]. examined the origin of the bubble formation depending on the wettability of the nano-channel surface using NEMD simulations. An external force was implemented on the metastable Lennard–Jones fluid (Ar), which was placed between two platinum surfaces at a temperature of 100 K. The modified LJ potential was implemented to represent the different solid–liquid interactions considering both the hydrophobic and the hydrophilic domains. The formation of the bubble varied depending on the type of surface used. Homogeneous nucleation was observed for hydrophilic surfaces, whereas heterogeneous nucleation was observed, and bubbles started forming on the solid surface. The Young–Laplace equation failed to describe the temperature and pressure inside the nano-bubble considering the macroscopic nature of the equation.

A very similar study was conducted by She et al. [106], where the surface was modified to form cavities.

Figure 9a depicts the molecular structure of a vapor bubble inside a solid cavity surface. Figure 9b,c represents the formation of nano-bubbles for hydrophilic and hydrophobic bottom surfaces. The study suggests that the cavity at the bottom can increase the size of the bubble formation, and the bubble initially develops near the vicinity of the cavity rather than on the surface. A greater magnitude of the force is experienced by the Ar atoms along the *z*-direction for cavity-incorporated systems. It was also observed that decreasing hydrophilic interactions decreases the size of the bubble. On the other hand, due to the presence of a gaseous layer near the surface, for hydrophobic surfaces, the cavity feature becomes irrelevant, which is established from the knowledge of nucleate boiling experiments.

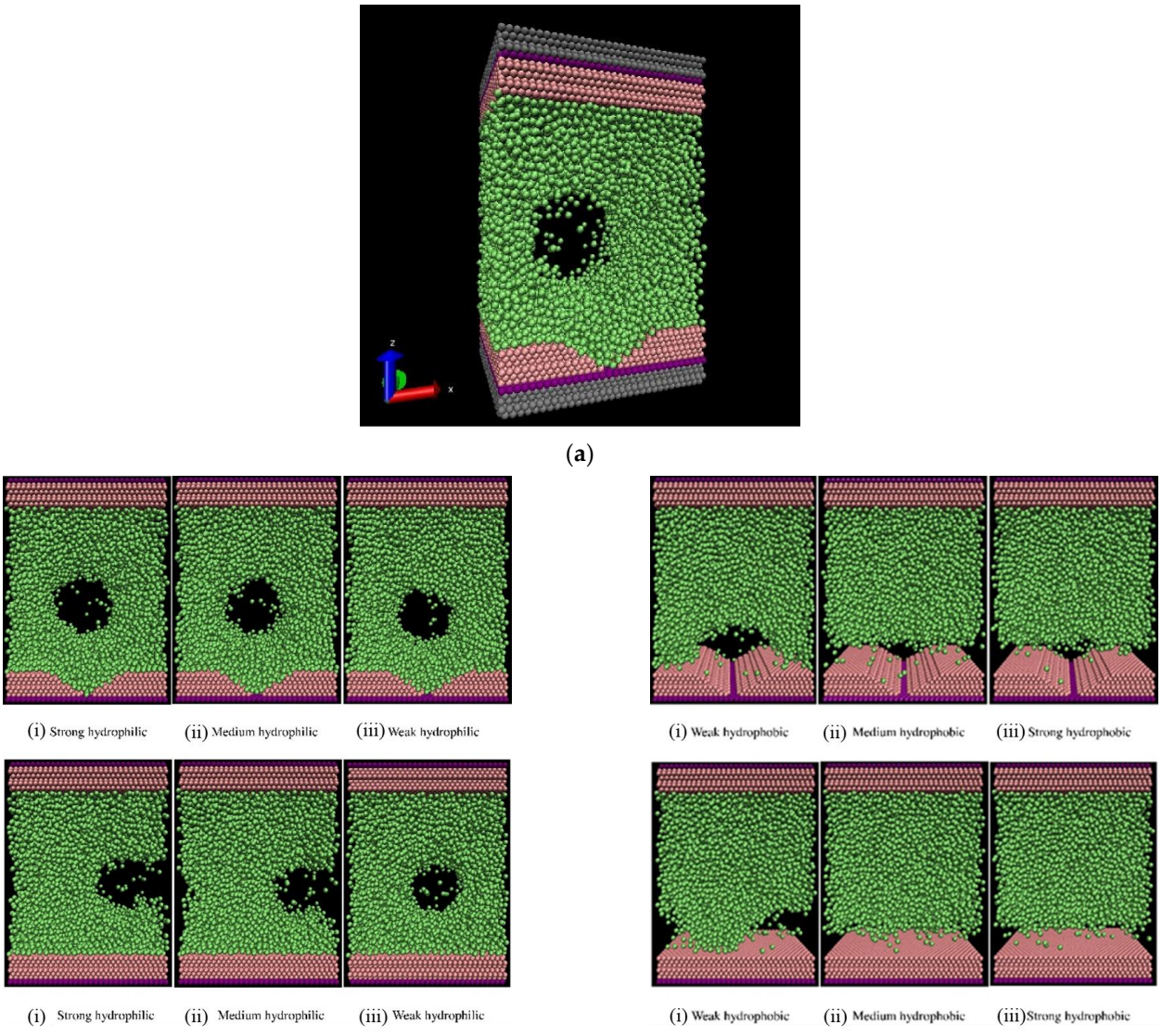

Figure 9. Bubble dynamics at the solid–liquid–vapor interface, and results on the variation of the hydrophobic and hydrophilic nature of the solid surface. (**a**) Initial condition after equilibration for argon molecules in between two parallel walls, (**b**) bubble formation in the presence of the hydrophilic bottom surface, and (**c**) bubble formation in the presence of the hydrophobic bottom surface. Reprinted with permissions from She et al. [106].

3.2.5. Droplet Coalescence

Droplet coalescence is crucial for several natural and industrial processes. Water harvesting through condensation methods, coating technologies, the formation of droplets in sprays and aerosol, viscous sintering, inkjet printing, emulsion stability, and the thermal management of microelectronic devices are some of the areas where the droplet coalescence process is used extensively. Coalescence is the phenomenon where two or more bubbles or liquid droplets merge to form a bigger entity of a bubble or liquid. There are two major stages of coalescence [107], (a) the joining of the droplets and (b) the growth of the liquid bridge. The thermal motions at the interfaces of the droplets create thermal capillary waves along with the surface force, which restricts the increase in the interfacial area to form a coalesced droplet. Several experimental and MD simulations have been performed to understand the dynamics at the interface of the two droplets during coalescence. Roy et al. [108] used NEMD simulations to investigate the effect of the relative distance between the droplets and concluded that the relative coalescence position abides by a power law, with dependence on the ratio of the parent droplets. Several studies present in the existing literature demonstrate the effect of parameters, such as the viscosity, interaction parameters of the droplet, and electric field direction, on the coalescing droplets. However, the effect of temperature variation is discussed rarely. Yi et al. [109] performed experimental work by colliding binary droplets on hydrophobic surfaces. The increase in temperature of the drops reflected a higher probability of coalescence. The major limitation of this study was that the condition of varying temperatures of the droplets was ignored, which is a very realistic scenario and important for liquid metals. The study of liquid metals requires a detailed understanding of the hydrodynamics of the droplets. Li et al. [110] used MD simulations to understand the coalescence process of two lead droplets on a graphene surface for different temperatures. This study is specifically important for the metallurgical industry. The two considered cases in this study were (a) an equal temperature of the nanodroplets at a different environment temperature and (b) different temperatures of the nanodroplets. The study suggests that the nano drops after mixing can be of three types, namely the uniform type, segregation type, and wrapped type, as presented in Figure 10. The type is highly dependent on the temperature difference and the absolute temperature of the cold droplet. Goudeli recently simulated gas-phase nucleation processes using AMD with reactive force fields. Recent studies show the influence of various external factors, like the temperature [110] and electric fields [111], on droplet coalescence.

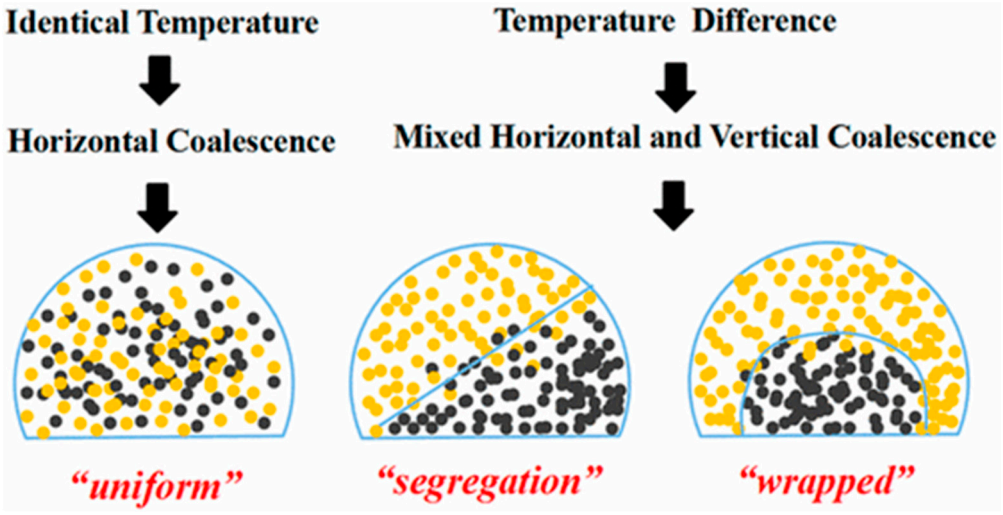

Figure 10. The three modes of coalescence, namely uniform, segregation, and wrapped. Reprinted with permissions from Li et al. [110]. Yellow dots represent the molecules of the nanodroplet at a high temperature whereas the black dots represent the molecules of the nanodroplet kept at a relatively low temperature.

3.2.6. Thin Film Evaporation at the Solid–Liquid–Vapor Interface

The two-phase heat transfer process utilizes the latent heat of the vaporization to dissipate heat for a given system. Micro/nanostructured surfaces have been implemented to increase the heat transfer coefficients and the critical heat flux of the system for boiling experiments. There are several explanations for the mechanism of increased critical flux, such as an elongated contact line, enhanced bubble departure frequency, enhancement of nucleation site densities, and microlayer evaporation. Among them, microlayer evaporation via wicking is the most widely accepted mechanism [112]. The major objective of the thin liquid film evaporation is to deliver liquid to the heated surface. The evaporating region is divided into three zones [112], as shown in Figure 11, namely the (a) nonevaporating film region, (b) evaporating thin film region, and (c) intrinsic meniscus region. The non-evaporating region is the zone where liquid–solid interactions are strong and the evaporation gets suppressed, in the thin film region an excess pressure known as the disjoining pressure dominates, and in the intrinsic meniscus region, the capillary forces dominate. This disjoining pressure rises rapidly as the film thickness decreases, and its gradient, caused by the thickness variation of the evaporating meniscus, causes the liquid to flow from the intrinsic meniscus to the evaporating thin film region, resulting in high heat flux in the evaporating thin film region. A detailed mathematical derivation of the phenomenon was presented by Hu et al. [113], which was validated through MD simulations. The study was to understand the effect of disjoining pressure for a thin film of water adsorbed on a gold surface. The EAM potential was used to simulate the effect of the interaction among the gold atoms, and the TIP4P-Ew water model was used for water–water interactions. The disjoining pressure was calculated in the absence of electrostatic interactions between gold and water to find them in great agreement with the classical disjoining pressure theory. The electrostatic-induced disjoining pressure was higher and was in a similar trend for experimentally observed polar liquid thin films.

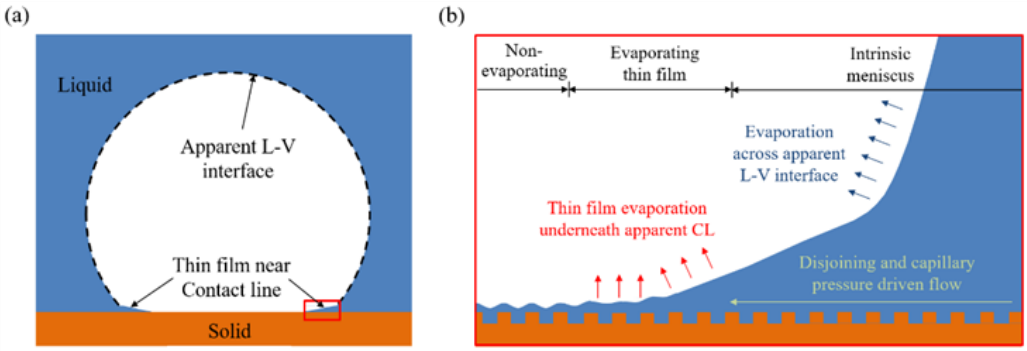

Figure 11. Representative schematic of thin-film evaporation. (**a**) Bubble during nucleate boiling, and (**b**) enlarged view of the contact line region on a nanostructured surface. Reprinted with permissions from Hu et al. [112].

Hu et al. [114] also performed NEMD simulations to understand the effects of nanopatterning on the Kapitza resistance at the liquid–solid interface during boiling. The nanopatterns were modified by their height and width-to-spacing ratio. The study depicted that phase change does not affect the Kapitza resistance, but the Kapitza resistance decreases with the increasing height of the nanopatterns and the width-to-spacing ratio. Figure 12 summarizes the various steps of MD simulations and the conventional systems studied for various micro and nanoscale thermal transports.

3.3. Miscellaneous Works

Machine learning (ML) has expanded its usability in the fields of image recognition [115], structural biology [116], cosmology [117], and healthcare [118,119]. Along with the direct application, ML is also used in improving the force field [120,121] and time economic prediction of MD simulations [122–125]. Ma and Dinner [126] in 2005 used

artificial neural networks to model a reaction coordinate from a set of MD trajectory data. The field of MDs is constantly evolving and is growing in parallel with several machine learning and deep learning algorithms that efficiently reduce the computational costs of calculation-intensive MD simulations. MD simulations are limited by the accuracy of the force fields [127]. Force fields are the interactions between the molecules present in a system where the electronic configurations are not considered and are fitted based on certain empirical equations. In principle, the most accurate way to obtain these forces is by numerically solving the Schrodinger equation (SE) [128], but the solution beyond two-body systems is computationally demanding. In such scenarios, mixed quantum mechanical/molecular mechanic (QM/MM) [120,121] treatments are performed where the SE is solved for a small part of the system with high accuracy. This approach also loses its efficiency when the treatment of the many-body interaction becomes important. Therefore, it is not always pre-determinable, where the modifications in the force field are required when the number of molecules in the system increases beyond a certain value [127,129,130]. This is where ML comes into the picture, where neither the accuracy of the ab initio nor the efficiency of the classical force fields is compromised. ML models broadly aim to learn the functional relationship between the input data and the output results from the patterns and structures in the data. A properly trained model can capture the underlying quantum mechanical rules [131,132] even without numerically solving the complicated SE. The ML-based models have shown very high efficiency and accuracy in a variety of molecular systems by learning the traditional semi-empirical methods along with the ab initio data [129,133]. The determination of several thermal transport properties of solids has been conducted using machine learning methods [125]. Quenching in aperiodic super-lattices using machine learning and thermal transportation in copper–water interfaces using deep learning methods were studied recently [122–125]. Several detailed reviews [134–138] have depicted the applicability of ML, ANN, and deep learning in the field of MD and ab initio-based simulations where a detailed description of the mathematical backgrounds is provided. Heat transport in non-metallic systems occurs via phonons, which have a distribution of frequencies and mean-free paths. Two length scales are majorly important in phonon dynamics, one is the phonon wavelength and the second is the mean free path of the phonon. These two parameters largely depend on the material and temperature of the system. If the system size is comparable with the mean free path of the phonon, then phonon ballistic transport phenomenons are considered, and if the system size is further reduced, then the wave nature of the phonons is considered. Several first-principle techniques are used to study the phonon dynamics, and a detailed review of this was performed by Bao et al. [139]. Carbon nanotubes are simulated using Phonon Green's function simulations, the determination of thermal conductivity of graphene using various quantum methodologies and non-equilibrium green functions [140]. Ballistic thermal transportations in 2D and 3D quantum structures [141], and hydrogenation and nitrogenation effects on the thermal conductivity of silicon nanowires [142] are also studied in detail. With the recent growth of nanocomposites as good thermal management materials, Tian et al. [143]. performed NEMD simulations to determine the thermal conductivity of nanocomposites and the effect of the orientation and arrangement of the nanoparticles on the composite.

A review of the various models and methodologies that are used in MD simulations to understand thermal transportation at the nano and microscale is presented in this section. In the next section, a brief review of different classical theories and different experimental methods that are being used in nano and microscale thermal transportation will be discussed.

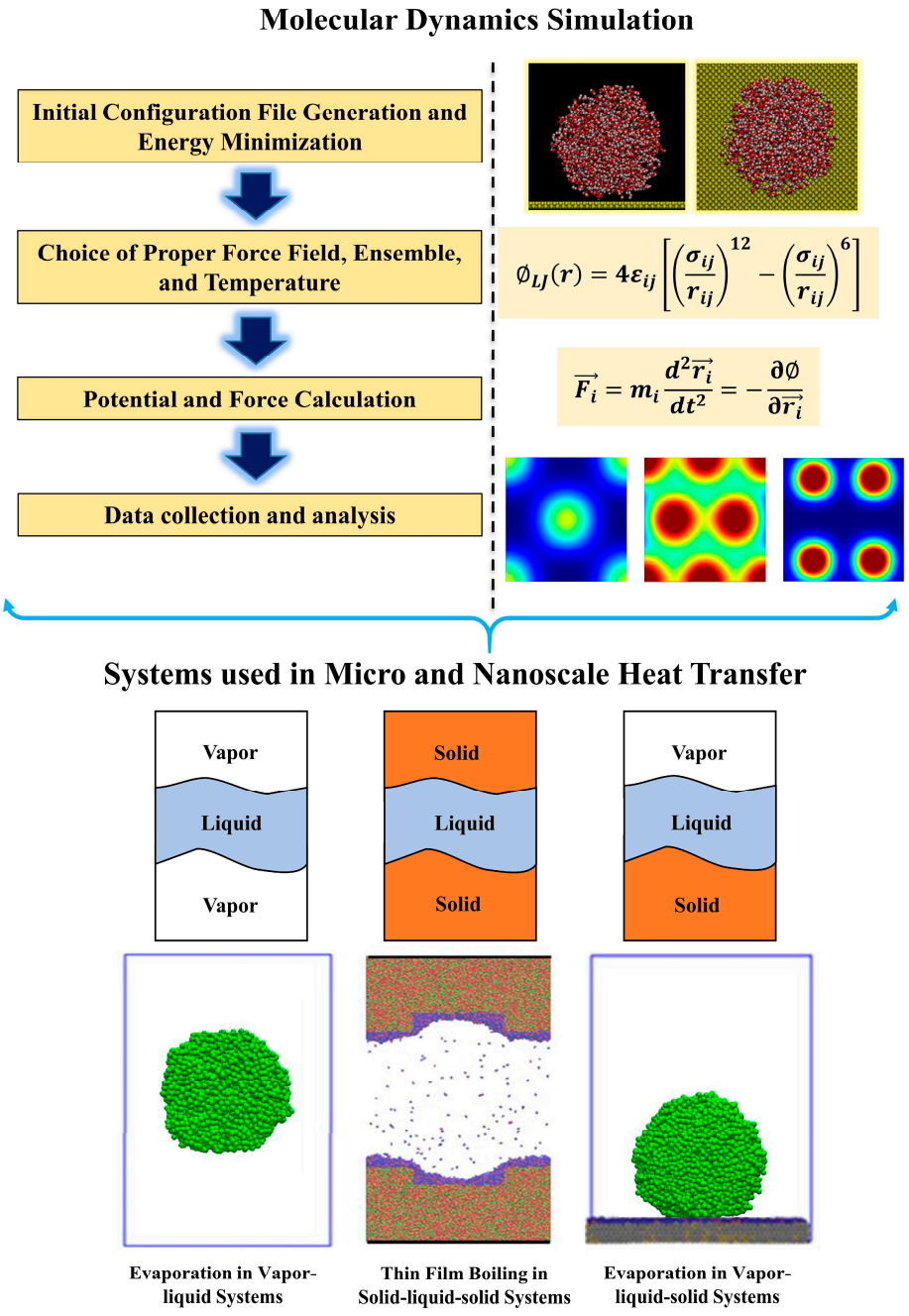

Figure 12. The overall process for the implementation of MD simulations for micro and nanoscale two-phase thermal transport problems.

4. Nanoscale Thermal Transport Theories and Experiments

Understanding heat transfer in nanoscale devices and systems is vital for designing and understanding its effects on nanoelectronics, thermoelectric materials, and heat management in nanoscale devices. Classical theories, such as Fourier's law, fail to explain energy transport at micro and nanoscale levels. Hence, fundamental statistical physics equations are used for the improved understanding of the energy transport at these scales. Two of the most popular models are the Boltzmann transport equation (BTE) and the phonon Boltzmann transport equation, which will be discussed briefly in upcoming sections. These equations use distribution functions to describe the interaction of a particle system with its surrounding environments.

4.1. Statistical Behavior of Nanoscale Transport Processes

Multiple transport theories can be used to explain heat transfer in the nanoscale. Before diving deep into the thermal transport theories, it is desirable to understand the various key factors that govern thermal transport at the nanoscale.

4.1.1. Phonon Transport

As discussed briefly in the previous section, phonons represent the discrete quantity of energy that is proportional in magnitude to the frequency of the lattice's vibration and is responsible for the transportation of heat energy in solids. It is an essential factor to be considered while dealing with the nanoscale, specifically in scenarios where the mean free path of the phonons becomes much smaller than that of the structure's characteristic length. Many theoretical models have been developed to describe phonon transport that takes place in nanoscale systems. Two such popular models are the Boltzmann transport equation (BTE) and the phonon Boltzmann transport equation [144]. The Boltzmann transport equation (BTE) is a fundamental equation in statistical physics that describes how the distribution function of a system of particles (such as electrons, phonons, or photons) evolves in response to their interactions with their environment. This equation provides a fundamental framework that can be used to study the transport of the particles, including their respective energies, momentum, and spatial distribution; mathematically, BTE is represented by the following:

$$\frac{\partial f}{\partial t} + v \cdot \nabla_r f + F \cdot \nabla_p f = \left(\frac{\partial f}{\partial t}\right)_{coll} \tag{14}$$

In Equation (14), $f = f(r, p, t)$ represents the probability density distribution of particles at their positions (r) with their respective momentum (p) with time (t); $\frac{\partial f}{\partial t}$ represents the time-derivative distribution function; v is the particle velocity; F is external forces acting on the particle; ∇_p and ∇_r represent gradients for momentum and position, respectively; and $\left(\frac{\partial f}{\partial t}\right)_{coll}$ represents the particle's collision (interactions and scattering) within the system.

4.1.2. Size Effects

Thanks to the modern advancements in nanotechnology, devices/structures with characteristic dimensions in the order of a few nanometers can be synthesized. Multi/single-walled nanotubes, carbon nanowires, and graphene nanosheets are some of the few examples of these structures [145]. Thermal transport is highly sensitive to the scale and dimension of the system. With a reduction in dimensions, the population and density of phonons present in the system will decrease, promoting alterations in thermal conductivity and phonon scattering. The effect of the system size in the nanoscale can be defined in two ways, i.e., (a) when phonons are treated as particles, and (b) when phonons are treated as waves. Different theoretical models, like the phonon confinement [146] and diffuse mismatch model [27,147], can be used to better explain the effect on thermal transport due to dimensional changes. However, when the mean free path of carriers becomes comparable to the material's dimensions, the Boltzmann transport equation (BTE) can be modified to incorporate effects due to confinement and boundary scattering, which also significantly affects heat transfer characteristics. In their research, Lindsay et al. [148] explained the length-dependent thermal conductivity of carbon nanotubes (CNTs) by solving the linearized BTE. They reported that the thermal conductivity of CNTs grows with the tube length, displaying a divergence behavior due to the vanishing dispersion of the long wavelength flexural phonon modes. They explained this behavior with the selection of criteria for Umklapp scattering that involves three phonons. For long nanotubes, a tiny cutoff frequency must be provided to decrease the diverging contribution from long wavelength flexural modes to obtain converged thermal conductivity. The armchair nanotubes have a similar length dependence. Another method to achieve convergent thermal conductivity is by introducing anharmonicity of a higher order [149]. Usually, in the case of an inelastic

phonon–phonon collision scattering process, the phase of the wave is destroyed during the collision, and if this occurs frequently inside the medium, the phonon wave characteristics can be ignored, and the transport occurs in the diffusion regime.

4.1.3. Boundary and Interface Effects

Phonics' interactions with the interface and boundaries of nanomaterials [150] highly affect heat transfer. The scattering of phonons affects heat conduction, strongly impacting the nanoscale thermal transport. Acoustic mismatch and diffuse mismatch models are some of the popular theoretical approaches that can be used to define and analyze the influence of boundaries and interfaces in thermal transport at the nanoscale. When phonons are treated as waves and their elastic interference exists with a rough interface, the transport is often assumed to be diffusive. Scattering phenomena at interfaces can potentially disrupt the phase of the scattered waves, and this is not solely due to intense elastic scattering. As a result, when an interface is rough, the dispersion of the waves can be considered phase-breaking, whereas a smooth interface tends to maintain phase coherence [151]. The roughness of the interface, relative to the wavelength, determines its classification as rough or smooth. Grain boundary scattering in nanowires also has significant impacts on thermal conductivity, its dependence on length, and surface roughness. Xiong et al. [152] proposed that a twinning superlattice nanostructure or resonant branching sub-nanostructures [153] can be used to effectively modify the length dependence of thermal conductivity in nanowires. Maire et al. [154] created smooth-surface silicon nanowires (SiNWs) using the top-down approach with dimensions between 0.5 and 7 m in length and 80 and 150 nm in transverse size. Their research shows that the roughness of the surface significantly dampens the effect of length. Also, grown SiNWs have a smooth surface with the presence of nanoscale roughness of around 2 nm. The thermal conductivity of these rough SiNWs is indifferent at room temperature due to the diffusive nature of phonon scattering on rough surfaces [155]. Scattering at both the transverse and the lateral boundary is part of the phonon–boundary interaction in nanowires. When photons hit a completely smooth surface and are reflected elastically, their momentum is not lost, and thermal resistance also remains unaltered. In this scenario, the effective mean free path for the phonon due to boundary scattering (λ_B) is constrained by the nanowire's length. However, λ_B depends on both the length and width of nanowires that have a rough surface and diffuse reflection at the lateral boundary. The thermal conductivity of nanowires depends on their length, and this information may be obtained using the Boltzmann transport theory.

This dependency on length, however, does not follow a power law. At the same time, low-dimensional materials have a thermal conductivity that strongly depends on their transverse size for two primary reasons [156,157]. Firstly, the nanowire effectively eliminates the thermal contribution of low-frequency (long wavelength) phonons. This results in strong temperature-dependent thermal conductivity, in low-dimensional materials. Secondly, compared to bulk materials, low-dimensional materials have a larger surface-to-volume ratio (SVR), resulting in enormous boundary/surface scatterings in the transverse direction. When the dimensions of a structure are comparable to or smaller than the mean free path, size effects come into play, and they are considered to exhibit classical behavior if the scattering at the interface is diffuse. Ye et al. [158] used the normal mode decomposition method to study the effects of the temperature, chirality, and edge dimension on spectral phonon properties of graphene nanoribbons (GNRs). Their study shows that the phonon relaxation time is unaffected by the edge chirality, whereas the phonon group velocity is strongly affected by the edge chirality. Thus, at room temperature, the thermal conductivity of the zigzag GNR is approximately 707 W/(m K), compared to 467 W/(m K) for the armchair GNR of the same width. The thermal conductivity drops dramatically as the width is reduced or the temperature is raised.

4.2. Applications of Micro/Nanoscale Heat Transfer

Nanoscale and microscale fabrication/modification hold immense potential and applications in several diverse fields. This section of the review will discuss some of the important applications, including Microfluidic devices, Micro/nano heat exchangers, heat pipes, Microprocessors and integrated circuits, Nanoelectromechanical systems (NEMS), and energy harvesters (Figure 13). The effect of nanoparticle introduction, bubble entrainment, surface modification, thin-film boiling, and evaporation on the overall heat transfer performance and transport behavior of the device is also discussed.

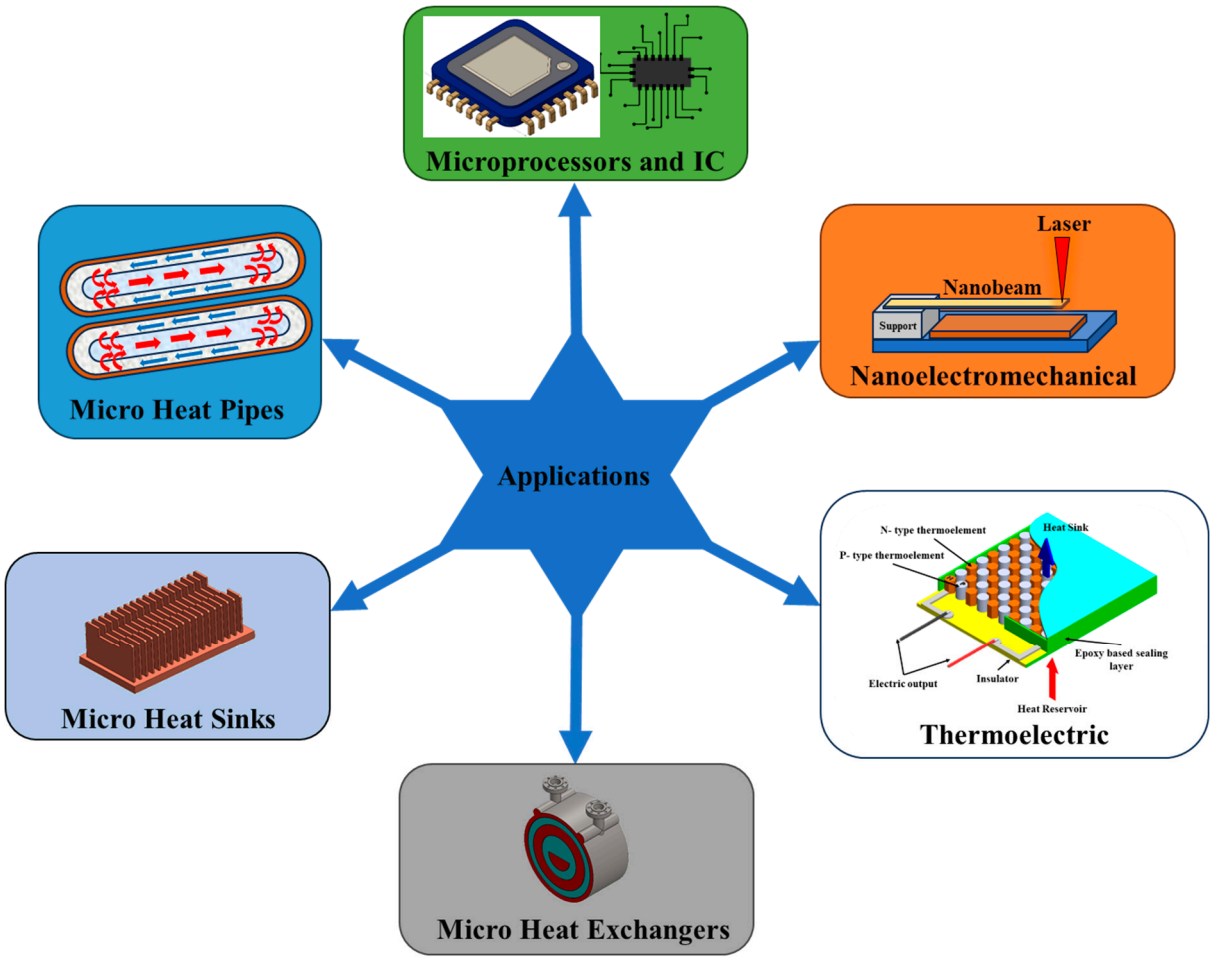

Figure 13. Applications of Micro/nanoscale heat transfer.

4.2.1. Microfluidic Devices

The efficiency and usefulness of microfluidic devices are significantly impacted by the transport and heat transfer effects. According to Squires et al. [159], a packet of fluid inside the microchannel behaves similarly to a droplet on a solid surface with a thermal gradient. However, the latter can shift as a result of the driving Marangoni stresses at the interface. Advection, diffusion, electrophoresis, and surface contacts are all examples of transport phenomena that can be harnessed in microfluidics to achieve highly tunable fluid and particle dynamics. The low Reynolds numbers inside a typical microchannel guarantee laminar flow and keep mixing to a minimum [159]. Diffusion, propelled by heat inside the microchannel, provides effective mixing and concentration gradients [160]. In the technique of electrophoresis, charged particles move in response to an applied electric field [161]. Fluid flow, adhesion, and analyte capture can all be improved by modifying or coating the surfaces [162].

The three modes of heat transport (conduction, convection, and radiation) are all present in microfluidic devices. The small diameters of microchannels facilitate conduction through solid walls and substrates [159]. As laminar flow predominates during convection, heat is dissipated and temperatures are kept more constant [160]. Radiation heat transfer is often insignificant in microfluidic applications but becomes important at high temperatures or with optically transparent materials [159]. Optimizing the design and performance of microfluidic devices requires a deep familiarity with momentum and heat transport in these systems. Im et al. [163] fabricated copper oxide flowers, like nanostructures, to enhance the nucleate pool boiling. They described how the large surface area-to-volume ratio of nanostructures promotes boiling via capillary wicking. The inclusion of CuO nanostructures in a smooth and micro-grooved surface resulted in an estimated 58% improvement in the critical heat flux (CHF), despite the nanostructures' relatively thin thickness of 3–4 μm. Chen et al. [164] used non-equilibrium MD (NMED) simulations to explore the transport behavior of water molecules inside a model carbon nanotube, which is validated qualitatively by conducting an infiltration experiment (pressure-induced) on carbon having nonporous arrangements in glycerine media. It has been found that the shearing stress between the nanotube wall and the water molecules is a crucial component in defining the nanofluidic characteristics. The effective shearing stress is both size-sensitive and fluid-flow-rate-dependent because of the nanoscale confinement. This finding demonstrates that the nominal viscosity of the confined liquid is substantially dependent on the flow rate and the tube size.

4.2.2. Introducing Nanoparticles

Increasing applications in biomechanics, science, nuclear industries, and chemical [165] sectors have boosted the research interest in nanofluid flows recently. Heat transfer effects in nanoelectronics devices and the changes induced in the thermal conductivity of nanocomposites, consisting of nanowires or nanoparticles embedded in a matrix material, are a few instances of engineering applications that demand a detailed investigation into transport processes in complex nanostructures [166]. Enhancing the effectiveness of heat transfer can be performed in several ways. The use of microchannels, the vibration of heat-transfer surfaces, and expanded surfaces are a few to mention. According to Kaneez et al. [167], while transporting fluids via hybrid nanostructures, the velocity of the fluid is a growing function of the mixed convection parameter, and floatation is aided by the buoyancy force. In addition to this, they reported that the interaction parameter between fluid velocity and hybrid nanostructures is highly crucial in determining the fluid flow behaviors within the nanoscale devices. Memory effects are time-dependent, and the restoration of the fluid's previous condition plays a crucial role in reducing the flow rate and the thickness of the boundary layer. Increasing the thermal conductivity of the working fluid is another way to boost heat transfer efficiency [168]. Small solid particles added to a fluid can improve its thermal conductivity due to the high thermal conductivity of solids. Water, oil, ethylene, biofluids, and lubricants laden with nanoparticles (size less than 100 nm) are all examples of nanofluids. Heat transmission using the nanofluids is improved due to the nanoparticles' increased thermal conductivity [169].

Nanofluids provide many advantages over more traditional solid–liquid suspensions, including a larger specific surface area, greater dispersion stability, lower pumping power requirements, and less particle clogging. Rashid et al. [170] examined the influence of nanoparticle loading on natural convection in a standard lid-driven square cavity with a stationary circular obstruction in the middle. They discovered that in a lid-driven square cavity with a fixed circular obstruction at its center, the shape of the nanoparticles affected the flow of the nanofluid within the cavity. They also reported that the velocity distribution, temperature distribution, and kinetic energy of the fluid in nano/microstructures are affected by different physical characteristics, like the sphericity of the nanoparticles, the Richardson number, and the Reynolds number.

4.2.3. Micro/Nano Heat Exchanger

Research related to micro/nano heat exchangers has seen a rise in interest due to its potential to improve heat transfer processes in a variety of applications [171]. Micro and nanoscale heat exchangers are observed to be effective in managing heat and energy transfer in microcircuits [172]. Due to size-dependent effects and enhanced surface-to-volume ratios, energy and heat transmission at this scale are distinct from the traditional macroscale [172]. Energy transfer in micro/nano heat exchangers is primarily governed by two mechanisms, i.e., conduction and convection [173]. However energy transport at these scales is usually associated with multiple nonequilibrium processes due to the similarity in the system length scales with the molecular mean free path and process time scales being lower than the relaxation time [174].

At the micro and nanoscales, conduction is the dominant route of heat transfer, as it involves the exchange of thermal energy through physical contact between adjacent particles. Generally, phonons are the primary heat-conducting particles in micro/nano heat exchangers since they are the quantum mechanical representations of lattice vibrations [175]. Phonons transmit heat in a wavelike fashion, allowing for effective heat transfer. Manipulating phonon transport to improve heat transfer is a major feature of micro/nano heat exchangers. To adjust energy transport at the micro/nanoscale, the thermal conductivity of the lattice can be modified with the inclusion of nanoparticles [176], nanostructures can be introduced, and surface modifications, like coatings and nano-patterns, can be implemented [177,178].

Increasing the efficiency of energy transfer is largely dependent on convective heat transfer in micro/nano heat exchangers [172]. The transfer of heat, carried by the motion of fluid, from one area to another, is known as convection. Approaches, including the use of microchannel or nanoporous structures, micro/nanofluids, and surface changes, are used in micro/nano heat exchangers to improve convective heat transfer [179,180]. Microchannels and nanoporous shapes improve convective heat transfer as they increase the surface area accessible for heat exchange and facilitate fluid mixing [179,181]. Due to their high thermal conductivity and higher convective heat transfer coefficients, nanofluids can improve heat transmission [182,183]. The flow behavior and heat transfer properties inside the micro/nano heat exchanger can also be affected by surface modifications with hydrophilic or hydrophobic coatings [184,185].

Electronic cooling, energy conversion systems, medicinal devices, and microreactors are just some of the many uses for micro and nano heat exchangers [186]. There are many advantages of using micro/nano heat exchangers. The small form factor, reduced weight, and enhanced heat transfer efficiency of micro/nanoscale heat exchangers make them suitable candidates for conventional heat exchangers for applications in the field of microelectronics. Their micro/nano size features help them with enhanced transport capabilities by promoting effective heat and energy transport, along with reduced power consumption, leading to a boost in the overall performance of the device or assembly.

4.2.4. Bubble Entrainment

Bubble entrainment significantly alters the transport and heat transfer characteristics when dealing with micro and nanostructures. As bubbles form and move inside these structures, fluid flow patterns, interfacial regions, and heat transport pathways are all affected. Understanding the mechanisms and results of bubble entrainment thus becomes an important parameter to study for maximizing the performance of micro and nanostructures. Bubble entrainment may arise as a result of three distinct mechanisms, namely nucleation, growth, and separation. Nucleation causes tiny bubbles to form, and it is commonly triggered by a localized decrease in pressure or rise in temperature in microstructures. Bubble nucleation, on the other hand, can take place spontaneously in nanostructures due to the high surface energy and curvature effects [187].

Inside the microchannels, bubbles are usually surrounded by the heated walls [188], and their presence has a significant impact on the thermal transport characteristics within the micro and nanostructures. Bubbles enhance mixing and mass movement by altering

the flow patterns of the fluid. Induced convective motion helps in the transport of particles, molecules, or heat [189] and is responsible for improving the overall performance of micro/nano systems. Changes in the interfacial area between the fluid and the solid caused by bubble entrainment can also affect the transport across surfaces. Chemical reactions and adsorption are impacted by an increase in the interfacial area [174,190].

Bubble entrainment also has a major effect on heat transfer in micro and nanostructures. Bubbles enable a process called nucleate boiling, which is another way heat is transferred via the liquid–vapor-phase transition. When bubbles form and expand at the liquid–vapor contact, they absorb heat and cool the surrounding liquid. However, as a bubble breaks apart, the latent heat of vaporization is released, causing localized heating [191]. Depending on the conditions, this dynamic heat transfer mechanism can either facilitate or hinder heat dissipation in micro and nano environments [192].

Therefore, the study of bubble entrainment in nano and microstructures has significant potential applications in several different disciplines. The use of bubble entrainment in electronic cooling improves reliability by reducing the effects of heat buildup and eliminating hotspots [193]. The efficiency of drug administration in biomedical applications is enhanced by bubble-induced fluid movement, which aids in mixing and transporting medicines [194]. The entrainment of bubbles speeds up chemical processes in microreactors while reducing the volume of reactants needed [195]. These examples highlight the need for the knowledge and control of bubble entrainment for optimizing the performance of micro and nanostructures.

4.2.5. Energy Conversion at the Nanoscale

Nanoscale systems involve objects or materials with a size of nanometers (10^{-9} m). Matter behaves differently at micro and nano scales, offering new energy conversion applications. Nanomaterials' high surface area-to-volume ratios and quantum effects can improve electrical conductivity, catalytic activity, and light absorption. Nanosolar cells use the photoelectric effect to turn sunlight into power [196]. Quantum dots and nanowires absorb light and generate an electric current in these devices. Nanoscale thermoelectric materials are also used for energy conversion. Based on the Seebeck effect (Figure 14a), these materials can convert waste heat into electrical energy or vice versa. Researchers are working on improving the nanomaterial thermoelectric characteristics and energy conversion by manipulating their structure and composition. Nanoscale mechanical devices, like nanoscale motors or generators, can turn mechanical energy into electrical energy or vice versa. These devices convert energy by influencing molecules or nanoparticles using nanoscale friction, piezoelectricity, or magnetism. Piezoelectric materials, like polyvinylidene fluoride (PVDF) [197–199], lead zirconate titanate (PZT), commercial transducers, [200] performance poly(methyl methacrylate) (PMMA), and graphene oxide (GO) [201], have been used to harvest energy from the raindrop impact. Recently, people started working on a waterproof and fabric-based multifunctional triboelectric nanogenerator (WPF-MTENG) [202] that shows promising results for energy harvesting even from very small external perturbations. The huge scope of improvements that can be made in the field of rain droplet-based nanogenerators motivated these studies. Piezoelectric nanogenerators (PENG) utilize the lost mechanical energy released in the form of noise, pulsations, airflow, and human body movements [203]. These PENGs can cooperate with flexible electrodes to harness electrical energy. Soin et al. [204], in their research, used the piezoelectric properties of polyvinylidene fluoride (PVDF) to impart piezoelectric properties to a nano-woven fabric. The resultant piezoelectric cloth generates an output electric power density in the range of 1.10–5.10 μ Wcm^{-2} when a pressure of 0.02–0.10 MPa is applied. Kang et al. [205], in their research, reported that doping conventional piezoelectric material could enhance its electrical performance for its applications in flexible nanogenerators. The researchers also reported that the 5 mol% doping of lanthanum in zinc oxide shows an increase in an output voltage of 0.9 V compared to undoped material. Doping increases the carrier mobility and produces a much higher output current (8 nA) compared to an undoped (1.6 nA) one. The

importance of droplet dimensions in energy harvesting is reported by Tinaikar et al. [206] marking it as a key parameter to study. They also explained that recoverable energy from rainfall depends directly upon the size of the piezoelectric membrane and the size of the raindrop. The amount of energy that can be harvested per drop varies from 2 µJ to 1 MJ. Nanoscale energy harvesters, like piezoelectric nanogenerators, transform mechanical vibrations into electrical energy. Nanobatteries and supercapacitors are developed for high-energy-density, fast-charging energy storage.

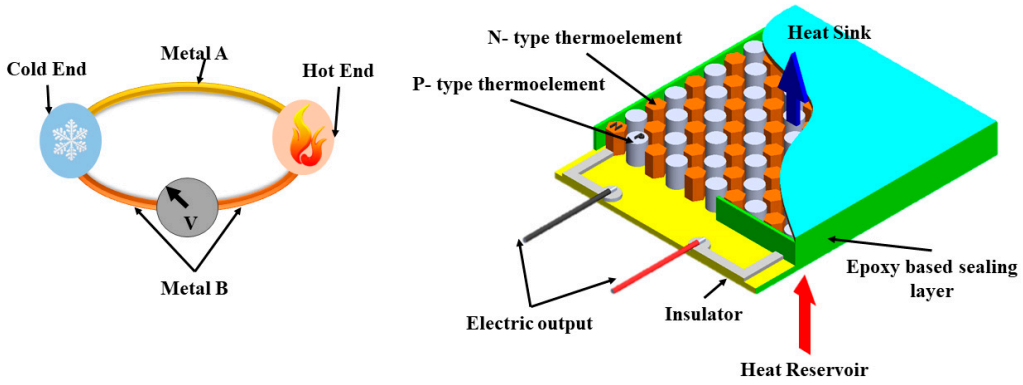

Figure 14. Schematic of (**a**) Seebeck effect, and (**b**) thermoelectric nanogenerator assembly.

4.2.6. Thermoelectric Energy Conversion

A thermoelectric nanogenerator (TENG) works on the principle of the Seebeck effect. A TENG can produce electricity from heat if there is a temperature gradient within the device (Figure 14b). The majority of the charge carriers (holes in p-type materials and electrons in n-type materials) will diffuse from the heated side to the cooled side when one side of the material is heated and the other is cooled. The accumulation of charge carriers at the cold end is a consequence of this diffusion process. When charge carriers accumulate at one end of a semiconductor, the resulting potential difference is proportional to the temperature difference between the two ends of the material [207]. Thermoelectric energy conversion is a process that involves the movement of charge carriers, like electrons or holes, as well as the transmission of energy across a temperature gradient. It is based on electronic and ionic transport principles, as well as electronic and lattice thermal transport. Charge carrier transport refers to the flow of charge carriers across the material's electronic band structure [208]. The carrier concentration, carrier mobility, and effective mass are all important elements in electronic transportation. Doping can boost the carrier concentration by introducing impurities into the crystal lattice [209]. Adding donor atoms, like phosphorus, to silicon, for example, increases the number of free electrons available for conduction. Carrier mobility, or the ease with which charge carriers can travel, is governed by scattering mechanisms, crystal defects, and temperature. The electrical conductivity of thermoelectric materials can be improved by optimizing carrier mobility. The inertia of charge carriers is determined by the effective mass. A lower effective mass allows for simpler passage through the lattice, resulting in improved electrical conductivity [208].

Another significant mechanism in thermoelectric materials is ionic transport. It involves ion mobility inside the material, which can have a considerable impact on thermoelectric characteristics, especially in materials with high ionic conductivity [210]. For example, the transport properties of oxide-based thermoelectric materials rely on oxygen ion migration. Understanding and regulating electrical and ionic transport processes is critical for improving thermoelectric performance.

In thermoelectric energy conversion, energy transmission processes are equally significant. Electronic thermal transport is the transfer of heat via charge carrier motion [208]. To reduce heat dissipation, it is preferable to have low electrical thermal conductivity. Reduced thermal conductivity can be achieved by reducing phonon–electron scattering. Increasing

the density of states around the Fermi level can impact charge carrier scattering rates, effectively lowering electronic thermal conductivity [211]. This is possible through band engineering or alloying procedures. The electronic heat conductivity of bismuth telluride (Bi_2Te_3), for example, is effectively lowered by inserting antimony atoms to form a solid solution [212].

Lattice thermal transport, on the other hand, refers to heat transfer via crystal lattice vibrations [208]. High lattice thermal conductivity is desirable in thermoelectric materials to promote efficient heat transport throughout the material. However, due to the interaction between charge carriers and lattice vibrations, achieving high electrical conductivity and low thermal conductivity at the same time is difficult. Phonon scattering is one method for lowering the lattice thermal conductivity. The introduction of atomic-level disorder, such as point defects or nanostructuring, can scatter phonons and obstruct their transmission resulting in a low thermal conductivity [213]. Superlattices and nanocomposites, for example, display greater phonon scattering and improved thermoelectric performance [214].

For instance, bismuth telluride (Bi_2Te_3) and lead telluride (PbTe) can be taken as examples to demonstrate the principles described above. Bismuth telluride is a popular thermoelectric material due to its high thermoelectric efficiency at room temperature [215]. In Bi_2Te_3, the charge carriers responsible for electrical conduction are holes, which are formed by doping with elements, such as antimony [212]. The electronic transport properties of Bi_2Te_3 can be optimized by carefully regulating the doping and band engineering. Lead telluride (PbTe) is another prominent thermoelectric material that performs well at high temperatures [216]. PbTe is a narrow bandgap semiconductor that, depending on the doping elements utilized, can exhibit both n-type and p-type electronic transport features. To improve phonon scattering, nanoscale features, such as nano inclusions or nanostructuring, can be added to diminish the lattice thermal conductivity [217]. Charge carrier transport and energy transfer processes are necessary for efficient thermoelectric energy conversion. Charge carrier movement is governed by electronic and ionic transport, while energy transfer is governed by electronic and lattice thermal transport. Researchers can improve the performance of thermoelectric materials for a variety of applications by studying and regulating these processes. To improve charge carrier transport and lower thermal conductivity, doping, band engineering, and nanostructuring techniques are routinely used. Examples of thermoelectric materials that demonstrate the success of these tactics are bismuth telluride and lead telluride. More research and development in this area is going on to advance thermoelectric energy conversion technologies.

4.2.7. Some Industrial Applications

(a) Microprocessors and integrated circuits

Recent advances in electronics and semiconductor processing have enhanced the usage of small and precise devices to deliver efficient and accurate performance. Microprocessors and integrated circuits are such unique small-scale devices that have temperature sensitivity and control where the proper thermal management of these systems becomes crucial for their optimal performance efficiency. In addition, the physical characteristics of these electronic parts are compact, and the available heat transmission surface area is small [218]. Consequently, efficient cooling calls for compact heat dissipation from these fragile substrates. The main aim of studying the heat transport in such devices is to know the maximum allowable temperature (100 °C for a typical semiconductor chip [219]) of the component to maintain efficient thermal control within their fictional limits. Intermetallic growth, corrosion, metal migration, and void formation are all thermally driven failure mechanisms that speed up as the absolute temperatures of a microchip rise [220]. Soldering can give rise to more cumulative fatigue per cycle at higher operating temperatures.

(b) Nanoelectromechanical systems (NEMSs)

Nanoelectromechanical systems (NEMSs) are nanoscale devices that blend electrical and mechanical functions for their use in various applications [221]. These NEMSs often

take the shape of cantilevers or doubly clamped beams in nanometer-scale dimensions. Active components are made of materials, like silicon, silicon carbide, carbon nanotubes, gold, and platinum, to name a few [222]. As micromachining and chip integration technology has advanced, the ability to accurately monitor temperatures in small packages has become increasingly important, not just in the diagnosis of potentially fatal diseases but also in cutting-edge industrial settings [223]. Micro-temperature sensors have received interest because of their small size [224], their ability to learn and adapt [225], and their high level of integration [226]. There is a growing need for miniaturized thermal resistance nanoelectromechanical systems for high-temperature testing [227] owing to technological progress and the success of industrialization. For instance, the manufacturing of a temperature-measurement device for the petroleum industry that requires the measurement in the path of the gas field must be efficient in measuring temperatures over 500 K [228]. A similar requirement of measuring high temperature [229] is found in the pharmaceutical industry, where temperature is monitored during the manufacture and sterilization of drugs. That is why refining the high-sensitivity thermal resistance temperature sensor's measurement interval is crucial. Table 2 below details some of the drawbacks of NEMS/MEMS devices, in addition to their many benefits.

Table 2. Advantages and disadvantages of NEMS/MEMS.

Advantages	Disadvantages
• Lower energy consumption and cost of fabrication	• Poor wear-resistant characteristics
• High replicability devices	• Highly prone to fracture
• Higher electrical conductivity and better ductility	• Toxic materials used for fabrication
• Lightweight devices	• Challenges related to handling nanoscale devices

(c) Microscale heat pipes and sinks

The use of microscale heat sinks, where the forced air or liquid coolant is integrated into the electronic package, is one of the most common responses to the problem of overheating in microscale devices [230]. Heat sinks do not function efficiently in high-temperature situations. Under these circumstances, utilizing the latent heat of the coolant, micro heat pipes can achieve higher heat transfer coefficients than micro heat sinks, making them increasingly useful. Microheat pipes have a hydraulic diameter between 10 and 500 μm [231], and their cross-sections are typically convex but cusped (e.g., a polygon). As the size of the region of interest requiring thermal control is reduced, the generated heat flux by the device shoots up [232]. The transfer of heat from a warm region of the heat pipe to the condenser takes place through microwicks or channels via the capillary force. Capillary pressure created by the device's acute corners helps in moving the condensate inside. The sharpness and number of the corners determine the rate of circulation of the working fluid and thus the heat transfer coefficient of the micro heat pipe. A reduction in the apex angle of the channel and the pipe length maximizes heat transfer [233]. Microheat pipes are a potential device for ensuring consistent temperatures and rapid local heat removal in miniature electronic components [234].

4.2.8. Effect of Surface Modification

Past decades have seen major strides in the field of efficient energy conversions in nanoscale systems due to the rise in the demand for alternative and sustainable energy sources. Surface modification includes modifying or imparting the material surface with special functional properties to enhance its desired applications. In the field of photovoltaics and catalysis, surface modification at the nanoscale has emerged as a potential way to achieve this goal. Photovoltaic devices, such as solar cells, modify surfaces to increase the efficiency with which sunlight is converted into electricity. Surface passivation is an efficient method for increasing energy conversion efficiency [235]. This process includes the deposition of a thin layer of insulating material onto the surface of the semiconductor

to decrease surface recombination and increase the charge carrier lifespan of the energy conversion system. To boost energy conversion, photovoltaic materials often undergo additional surface modifications, such as nanostructuring [236], which increases the area available to absorb light. Plasmonic nanoparticle integration on solar cell surfaces enables localized surface plasmon resonance (LSPR), which improves energy conversion efficiency by increasing light absorption and charge generation [237].

In the field of applied catalysis, surface modification is useful and is a critical process for many energy conversion technologies, including fuel and electrochemical cells. Surface modification provides a higher number of active sites to the catalyst surface, providing a large surface for the reaction and influencing the reaction kinetics [238]. Improving the adsorption properties of catalyst surfaces is another useful strategy for increasing the efficiency of fuel cell reactions, such as the hydrogen evolution reaction (HER) and the oxygen evolution reaction (OER) [239]. The catalytic stability and overall energy conversion efficiency can be enhanced by modifying the surface to create barriers or repel harmful species [235].

For possible applications in field-effect transistors, Pak et al. increased the photodetection characteristics by treating the surface with copper phthalocyanine (CuPc) [240]. They found that, when compared to pure MoS_2, the performance of CuPc/MoS_2 hybrid devices as photodetectors was significantly higher (~12.57% increase in the quantum efficiency). Moreover, such MoS_2 organic vertical hybrid structures hold great promise for their use in efficient photo-detecting devices and optoelectronic circuits. Nanoscale surface texturing can improve energy transfer efficiency, save significant energy, and cut global greenhouse gas emissions. Hu et al. [241] investigated the nanoscale surface modification's impact on heat transport during boiling and quenching. Using an aluminum surface with an anodized aluminum oxide (AAO) nanoporous texture finish, the critical heat flux was reported to be increased by 112%, and the Leiden frost point temperature was increased by 40 K, compared to a conventional aluminum surface. Because of the super hydrophilic surface property and abundance of nanoscale nucleation sites formed by the nanoporous surface, heat transport is improved on these materials. Unlocking the full potential of surface modifications for energy conversion at the nano/microscale can lead to multiple breakthroughs in the areas of nanotechnology and interdisciplinary research. Researchers can set the way for future advancements in energy conversion technologies by harnessing the power of surface modification and utilizing interdisciplinary collaboration.

4.2.9. Thin Film Boiling in Nano/Micro Materials

When it comes to nucleate boiling heat transfer, the crucial performance parameter relies heavily on the surface morphology, which can be made possible through the use of nanomaterials or nanofabrication. Improved boiling heat transfer methods have come a long way in recent decades. Hence, the proliferation of microscopic or man-made voids on a surface makes nanofabrication and surface enhancements a topic of intense research. Surfaces with improved micro- and nano-geometries can trap more vapor and gas, have a higher density of active nucleation sites and generate more heat from within. As a result of these enhancements, the boiling heat transfer coefficient was enhanced by decreasing the incipient wall superheat and boiling superheat [242,243]. The shape of the wetting liquid meniscus (governed by the disjoining pressure and capillary pressure) is highly critical for the heat transmission performance. As the film thickness is decreased and the structure depth increases, it is reported that the meniscus conforms more closely to the nano structure's surface [244]. Surface roughness at the nanoscale, when combined with a disjoining pressure effect, becomes extremely important. This surface roughness-induced evaporation results in a flatter evaporating meniscus profile. Hu et al. [245], in one of their studies, revealed that flow permeability has the most significant impact on thin-film evaporation. Their findings indicate that higher average surface roughness may also restrict evaporation and result in a steeper evaporating meniscus profile. It is essential to discover the precise surface roughness characteristics as that will decide the impact of

the disjoining pressure and flow permeability. Energy conversion, microelectronics cooling, boiling, perspiration, and self-assembly are only a few of the processes that rely on the evaporation from thin films. Transport processes along the contact line among liquid, vapor, and solid control the phase shift in these systems. Micro and nanoscale modifications to the surface chemistry and topography can significantly improve vaporization. For instance, Hassan et al., in one of their studies, explained the thin-film evaporation of argon over platinum-based nanostructures using molecular dynamic studies [246]. Their results show that the surface nanostructures and surface wetting characteristics enhance the heat-transfer capabilities of the surface. In the event of a perfectly wetting fluid, three distinct areas within the evaporating meniscus are observed as presented in Figure 15. The predecessor to the presumed contact line among the liquid, vapor, and solid is the adsorbed/nonevaporating film region. Because of the interplay of the attraction forces among the solid and liquid, vapor pressure, and temperature of the substrate, the thickness of this adsorbed/nonevaporating layer remains constant. The second region is known as the transition region where the liquid–vapor contact is significantly curved. During active evaporation, capillary and intermolecular forces direct the flow of liquid from the thicker region.

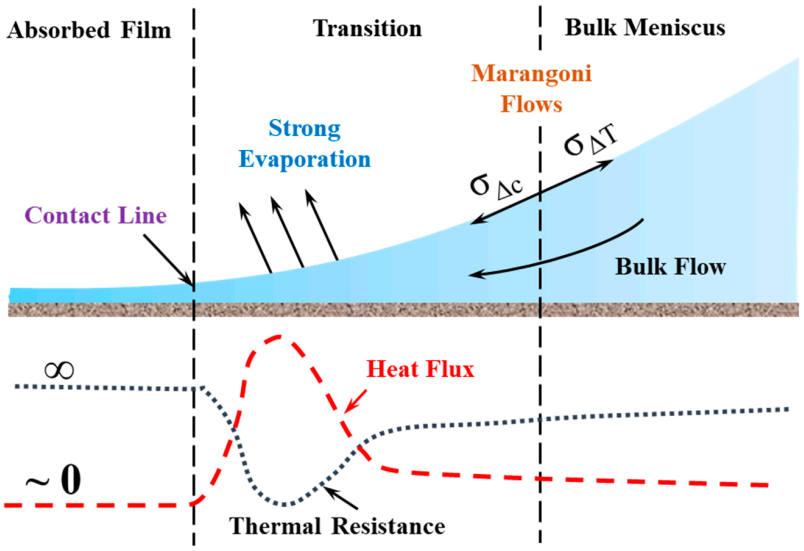

Figure 15. Variation in thermal resistance, and heat flux at the contact line regions for an evaporating meniscus.

The third region is the bulk meniscus, where the interface's curvature is essentially constant. This area serves as a reservoir, replenishing the transition zone with fluid. These three zones and their respective thermal resistances can be used to analyze the heat transmission process. A static meniscus has three resistances in series: (1) a conduction resistance through the solid substrate, which is typically small due to the high conductivity of the solid material; (2) a conduction resistance through the liquid, which is a linear function of the film thickness; and (3) a resistance to heat transfer across the liquid–vapor interface. For liquids with a high latent heat of vaporization or systems with a large liquid–solid interface area, this resistance to heat transfer across the liquid–vapor interface is the most important thermal resistance in the system [247].

4.2.10. Evaporation on the Nano/Micro Scale

The study of evaporation and condensation on the nano and micro scales presents a one-of-a-kind set of problems and reveals many fascinating behaviors as a consequence of quantum phenomena, surface interactions, and confinement. At the nanoscale, the principles of quantum mechanics predominate, leading to a departure from the behavior predicted by conventional physics. The evaporation of water from confined systems can be distinguished from the evaporation of water from the bulk by the fact that water in

confined systems can switch between vapor and liquid state throughout the process of evaporation. During the transition from the liquid to the gas phase, the system's entropy changes [248]. Ward developed a formula for the entropy production at an evaporating interface by applying the statistical rate theory [249]. They concluded that the interfacial entropy generation rate does not reach a minimum during the phase change process unless the system is closed. This was one of their findings. However, for open systems, the state of least entropy might be arbitrarily distant from the state of equilibrium, depending on the characteristics of the substances involved. In contrast, the meniscus region predominates in the evaporation from microscopic interfaces. The nanoscopic extension of the liquid–vapor interface starts to play a more significant role in the overall evaporation rate within nanoconfinement [250]. This is due to the availability of small free surface areas for evaporating liquids that are confined within the nanoconfinement. The thin film region that is evaporating has a modest thickness, which results in minimum heat transfer resistance across this layer. As a result, this region becomes an extremely high evaporating zone. Surface-to-volume ratios become important at the nano and micro sizes. At lower scales, due to transverse confinement, the electronic and phononic states are quantized leading to a finite level of spacing, resulting in distinct energy levels, which vary when compared to bulk materials. These factors can affect the thermodynamic properties of liquids, including their evaporation and condensation rates [251]. The stability of the liquid phase can also be affected by the surface energy of nanoparticles or nanostructured surfaces. Wetting qualities are heavily controlled by surface roughness and intermolecular forces. At the nanoscale, the influence of quantum processes, like Vander Waals [252] and Casimir–Polder [253] forces, on the adhesion and spreading of liquid molecules on surfaces become more pronounced. These effects can change the condensation rate by altering the process of droplet nucleation and growth. Water in confined nano/microscale systems can oscillate between the vapor and liquid state when it evaporates, as demonstrated by Xu et al. [254]. When dealing with nano/micro confinements, factors pertaining to the creation of a high-curvature meniscus and those resulting from the proximity and interference of the liquid–solid and liquid–vapor interfaces, become crucial parameters to study [255]. The meniscus region dominates in evaporation from micro/nanoscopic interfaces, but the nanoscopic extension of the liquid–vapor interface begins to play a more significant role in the overall evaporation rate within the nanoconfinement as the free surface area available for evaporation for liquids in the nanoconfinement decreases.

The proximity to the intrinsic meniscus region and contributions from the capillary force causes the liquid–vapor interface to develop with a small curvature in the evaporating thin film zone. Due to the minimal thermal resistance across this layer, the evaporating thin film region is extremely evaporative [248]. Table 3 summarizes the various applications of micro and nanoscale heat transfer in industry and research.

Table 3. Applications of thermal transportation of micro and nanoscale devices.

Application	Key Parameter	References
Microfluidic devices	• Reynold's number • Shear stress • Surface tension of the fluid • Channel properties	Ref. [159]
Micro/nano heat exchanger	• Surface area • Thermal conductivity • Surface properties	Ref. [173]
Microprocessors and integrated circuits	• Temperature-sensitive • Soldering • Type of material	Ref. [218]

Table 3. *Cont.*

Application	Key Parameter	References
Nano-electromechanical systems (NEMS)	• Temperature • Thermal resistance temperature • Surface features • Morphology of device	Ref. [221]
Microscale heat pipes	• Temperature • Morphology • Capillary pressure	Ref. [230]
Microscale heat sinks	• Temperature • Coolant fluid • Mechanism (forced/natural)	Ref. [256]
Thermoelectric energy conversion	• Temperature gradient, • carrier concentration, mobility, and effective mass • Thermal conductivity	Refs. [207,208]

5. Conclusions and Future Outlook

The field of micro/nanoscale heat transport is divided based on the involved length scales into two major domains: (a) above the continuum length scale and (b) below the continuum length scale. Numerous theories have been developed to describe heat transport in these length scales. MD simulations have proven to be a powerful tool for explaining small-scale systems. MD simulations have revolutionized the field by enabling researchers to move into the molecular length scale domain while reducing the complexity and computational expenses of ab initio simulations. Thin-film evaporation, the formation of vapor bubbles, three-phase heat transfer, coalescence, and condensation are studied in detail but the results deviate significantly from experimental studies, which indicate a requirement for improved MD models. These deviations are mainly observed due to the spatiotemporal scale variations of the simulated systems with reality. The accuracy of MD simulations is also limited by the quality of the force fields (FFs), which can result in deviations from experimental data. Yet, with recent advancements in machine learning-based force fields and ab initio-based simulations, the efficiency of the outcomes has been improved. The accuracy of MD simulations depends on a variety of factors, including the choice of system length scales, the accuracy of the FF, and the adjustment of the tuning parameters. The construction of ML-based FFs is one of the most promising applications, to close the gap between the precision of ab initio approaches. The main aim is to discover the statistical relationship between chemical structure and potential energy without prior knowledge of fixed chemical bonds or related interactions. In recent years, the application of ML in computational chemistry has enabled significant advancements that were previously unfeasible due to the computational complexity of traditional electronic structure techniques. One of the most interesting applications is the creation of ML-based force fields (FFs), to reduce the gap between the precision of ab initio techniques and the efficiency of classical FFs, which will eventually help in developing better FFs for systems related to micro and nanoscale heat transfer. It is to be noted that experimental validations and the development of newer methodologies for MD simulations must go hand in hand to obtain a bigger and better picture of physics on a smaller scale.

Author Contributions: Conceptualization, S.C., H.H. and M.C.; methodology, S.C.; validation, S.C., H.H., P. and M.C; formal analysis, S.C., P. and M.C.; resources, S.C. and P.; data curation, S.C. and P.; writing—original draft preparation, S.C. and P.; writing—review and editing, S.C., H.H., P. and M.C.; supervision, M.C.; project administration, H.H. and M.C. All authors have read and agreed to the published version of the manuscript.

Funding: This research received no external funding.

Data Availability Statement: Not applicable.

Conflicts of Interest: The authors declare no conflict of interest.

References

1. Idumah, C.I. Recently emerging trends in flame retardancy of phosphorene polymeric nanocomposites and applications. *J. Anal. Appl. Pyrolysis* **2023**, *169*, 105855. [CrossRef]
2. Wang, D.; Lin, S.S.; Huang, S.Q.; Yin, Z.F.; Yang, H.Z.; Bian, P.Y.; Zhang, Y.L.; Dai, M.J.; Zhou, K.S. Research on high temperature wear resistance mechanism of CrN/CrAlN multilayer coatings. *Tribol. Int.* **2023**, *180*, 108184. [CrossRef]
3. Hamed, H.; Eldiasty, M.; Seyedi-Sahebari, S.M.; Abou-Ziki, J.D. Applications, materials, and fabrication of micro glass parts and devices: An overview. *Mater. Today* **2023**, *66*, 194–220. [CrossRef]
4. Yu, Y.; Ma, T.; Huang, H. Semiconducting Quantum Dots for Energy Conversion and Storage. *Adv. Funct. Mater.* **2023**, *33*, 2213770. [CrossRef]
5. Masuduzzaman, M.; Kim, B. Scale Effects in Nanoscale Heat Transfer for Fourier's Law in a Dissimilar Molecular Interface. *ACS Omega* **2020**, *5*, 26527–26536. [CrossRef]
6. Luo, T.; Chen, G. Nanoscale heat transfer—From computation to experiment. *Phys. Chem. Chem. Phys.* **2013**, *15*, 3389. [CrossRef]
7. Knepp, Z.J.; Masso, G.B.; Fredin, L.A. Efficiently predicting directional carrier mobilities in organic materials with the Boltzmann transport equation. *J. Chem. Phys.* **2023**, *158*, 064704. [CrossRef]
8. Fiorentino, A.; Baroni, S. From Green-Kubo to the full Boltzmann kinetic approach to heat transport in crystals and glasses. *Phys. Rev. B* **2023**, *107*, 054311. [CrossRef]
9. Pan, H.; Ding, Z.K.; Zeng, B.W.; Luo, N.N.; Zeng, J.; Tang, L.M.; Chen, K.Q. Ab initio Boltzmann approach to coupled magnon-phonon thermal transport in ferromagnetic crystals. *Phys. Rev. B* **2023**, *107*, 104303. [CrossRef]
10. Chang, C.W.; Okawa, D.; Garcia, H.; Majumdar, A.; Zettl, A. Breakdown of Fourier's Law in Nanotube Thermal Conductors. *Phys. Rev. Lett.* **2008**, *101*, 075903. [CrossRef]
11. Liu, Y.; Li, Y.; Shen, K.; Qiu, Y.; Xie, J. Further decrease of the thermal conductivity of superlattice through embedding nanoparticle. *Int. J. Heat Mass Transf.* **2023**, *203*, 123789. [CrossRef]
12. Li, D.; Wu, Y.; Fan, R.; Yang, P.; Majumdar, A. Thermal conductivity of Si/SiGe superlattice nanowires. *Appl. Phys. Lett.* **2003**, *83*, 3186–3188. [CrossRef]
13. Cahill, D.G.; Ford, W.K.; Goodson, K.E.; Majumdar, A.; Maris, H.J.; Merlin, R.; Phillpot, S.R. Nanoscale thermal transport. *J. Appl. Phys.* **2003**, *93*, 793–818. [CrossRef]
14. Biehs, S.A.; Rousseau, E.; Greffet, J.J. Mesoscopic Description of Radiative Heat Transfer at the Nanoscale. *Phys. Rev. Lett.* **2010**, *105*, 234301. [CrossRef] [PubMed]
15. Kloppstech, K.; Könne, N.; Biehs, S.A.; Rodriguez, A.W.; Worbes, L.; Hellmann, D.; Kittel, A. Giant heat transfer in the crossover regime between conduction and radiation. *Nat. Commun.* **2017**, *8*, 14475. [CrossRef] [PubMed]
16. Lu, L.; Yi, W.; Zhang, D.L. 3ω method for specific heat and thermal conductivity measurements. *Rev. Sci. Instrum.* **2001**, *72*, 2996–3003. [CrossRef]
17. Zhang, Y.; Zhu, W.; Hui, F.; Lanza, M.; Borca-Tasciuc, T.; Muñoz Rojo, M. A Review on Principles and Applications of Scanning Thermal Microscopy (SThM). *Adv. Funct. Mater.* **2020**, *30*, 1900892. [CrossRef]
18. Gomès, S.; Assy, A.; Chapuis, P.O. Scanning thermal microscopy: A review. *Phys. Status Solidi* **2015**, *212*, 477–494. [CrossRef]
19. Andrew NSmith, J.L.H. Thermal boundary resistance measurements using a transient thermoreflectance technique. *Microscale Thermophys Eng.* **2000**, *4*, 51–60. [CrossRef]
20. Stevens, R.J.; Smith, A.N.; Norris, P.M. Measurement of Thermal Boundary Conductance of a Series of Metal-Dielectric Interfaces by the Transient Thermoreflectance Technique. *J. Heat Transfer.* **2005**, *127*, 315–322. [CrossRef]
21. Fischer, M.C.; Wilson, J.W.; Robles, F.E.; Warren, W.S. Invited Review Article: Pump-probe microscopy. *Rev. Sci. Instrum.* **2016**, *87*, 031101. [CrossRef]
22. Antonio, K.A.; Schultz, Z.D. Advances in Biomedical Raman Microscopy. *Anal. Chem.* **2014**, *86*, 30–46. [CrossRef]
23. Bebb, H.B.; Williams, E.W. *Chapter 4 Photoluminescence I: Theory*; Elsevier: Amsterdam, The Netherlands, 1972; pp. 181–320. [CrossRef]
24. Xiong, Y.; Shepherd, S.; Tibbs, J.; Bacon, A.; Liu, W.; Akin, L.D.; Ayupova, T.; Bhaskar, S.; Cunningham, B.T. Photonic Crystal Enhanced Fluorescence: A Review on Design Strategies and Applications. *Micromachines* **2023**, *14*, 668. [CrossRef]
25. Maqbool, Z.; Hanief, M.; Parveez, M. Review on performance enhancement of phase change material based heat sinks in conjugation with thermal conductivity enhancers for electronic cooling. *J. Energy Storage* **2023**, *60*, 106591. [CrossRef]
26. Li, R.; Wang, J.X.; Lee, E.; Luo, T. Physics-informed deep learning for solving phonon Boltzmann transport equation with large temperature non-equilibrium. *NPJ Comput. Mater.* **2022**, *8*, 29. [CrossRef]
27. Reddy, P.; Castelino, K.; Majumdar, A. Diffuse mismatch model of thermal boundary conductance using exact phonon dispersion. *Appl. Phys. Lett.* **2005**, *87*, 211908. [CrossRef]
28. Noothong, W.; Suwannapan, S.; Thianpong, C.; Promvonge, P. Enhanced heat transfer in a heat exchanger square-duct with discrete V-finned tape inserts. *Chin. J. Chem. Eng.* **2015**, *23*, 490–498. [CrossRef]

29. Eid, M.R.; Al-Hossainy, A.F. Synthesis, DFT calculations, and heat transfer performance large-surface TiO_2, ethylene glycol nanofluid and coolant applications. *Eur. Phys. J. Plus* **2020**, *135*, 596. [CrossRef]
30. Alder, B.J.; Wainwright, T.E. Studies in Molecular Dynamics. I. General Method. *J. Chem. Phys.* **1959**, *31*, 459–466. [CrossRef]
31. Stillinger, F.H.; Rahman, A. Improved simulation of liquid water by molecular dynamics. *J. Chem. Phys.* **1974**, *60*, 1545–1557. [CrossRef]
32. Nielsch, K.; Bachmann, J.; Kimling, J.; Böttner, H. Thermoelectric Nanostructures: From Physical Model Systems towards Nanograined Composites. *Adv. Energy Mater.* **2011**, *1*, 713–731. [CrossRef]
33. Mingo, N.; Yang, L. Phonon transport in nanowires coated with an amorphous material: An atomistic Green's function approach. *Phys. Rev. B* **2003**, *68*, 245406. [CrossRef]
34. Sadasivam, S.; Waghmare, U.V.; Fisher, T.S. Phonon-eigenspectrum-based formulation of the atomistic Green's function method. *Phys. Rev. B* **2017**, *96*, 174302. [CrossRef]
35. Peraud, J.P.M.; Landon, C.D.; Hadjiconstantinou, N.G. MONTE CARLO METHODS FOR SOLVING THE BOLTZMANN TRANSPORT EQUATION. *Annu. Rev. Heat Transf.* **2014**, *17*, 205–265. [CrossRef]
36. Eringen, A.C.; Edelen, D.G.B. On nonlocal elasticity. *Int. J. Eng. Sci.* **1972**, *10*, 233–248. [CrossRef]
37. Eringen, A.C.; Wegner, J.L. Nonlocal Continuum Field Theories. *Appl. Mech. Rev.* **2003**, *56*, B20–B22. [CrossRef]
38. Wu, J.W.; He, J.T.; Lin, J. Nonlocal symmetries and new interaction waves of the variable-coefficient modified Korteweg–de Vries equation in fluid-filled elastic tubes. *Eur. Phys. J. Plus* **2022**, *137*, 814. [CrossRef]
39. Kiani, K. Vibration behavior of simply supported inclined single-walled carbon nanotubes conveying viscous fluids flow using nonlocal Rayleigh beam model. *Appl. Math. Model.* **2013**, *37*, 1836–1850. [CrossRef]
40. Kiani, K. Nanofluidic flow-induced longitudinal and transverse vibrations of inclined stocky single-walled carbon nanotubes. *Comput. Methods Appl. Mech. Eng.* **2014**, *276*, 691–723. [CrossRef]
41. Feng, Y.; Sato, Y.; Inoue, T.; Liu, M.; Chiashi, S.; Xiang, R.; Suenaga, K.; Maruyama, S. Drastically reduced thermal conductivity of self-bundled single-walled carbon nanotube. *Carbon* **2023**, *201*, 433–438. [CrossRef]
42. Keblinski, P.; Prasher, R.; Eapen, J. Thermal conductance of nanofluids: Is the controversy over? *J. Nanoparticle Res.* **2008**, *10*, 1089–1097. [CrossRef]
43. Iqbal, M.; Kouloulias, K.; Sergis, A.; Hardalupas, Y. Critical analysis of thermal conductivity enhancement of alumina–water nanofluids. *J. Therm. Anal. Calorim.* **2023**, *148*, 9361–9389. [CrossRef]
44. Butler, K.T.; Davies, D.W.; Cartwright, H.; Isayev, O.; Walsh, A. Machine learning for molecular and materials science. *Nature* **2018**, *559*, 547–555. [CrossRef]
45. Souza, P.C.T.; Alessandri, R.; Barnoud, J.; Thallmair, S.; Faustino, I.; Grünewald, F.; Patmanidis, I.; Abdizadeh, H.; Bruininks, B.M.H.; Wassenaar, T.A.; et al. Martini 3, a general purpose force field for coarse-grained molecular dynamics. *Nat. Methods* **2021**, *18*, 382–388. [CrossRef] [PubMed]
46. Mahadevi, A.S.; Sastry, G.N. Cation–π Interaction: Its Role and Relevance in Chemistry, Biology, and Material Science. *Chem. Rev.* **2013**, *113*, 2100–2138. [CrossRef] [PubMed]
47. Fischer, J.; Wendland, M. On the history of key empirical intermolecular potentials. *Fluid Phase Equilib* **2023**, *573*, 113876. [CrossRef]
48. Mark, P.; Nilsson, L. Structure and Dynamics of the TIP3P, SPC, and SPC/E Water Models at 298 K. *J. Phys. Chem. A* **2001**, *105*, 9954–9960. [CrossRef]
49. van der Spoel, D.; van Maaren, P.J.; Berendsen, H.J.C. A systematic study of water models for molecular simulation: Derivation of water models optimized for use with a reaction field. *J. Chem. Phys.* **1998**, *108*, 10220–10230. [CrossRef]
50. Jian, Z.; Kaiming, Z.; Xide, X. Modification of Stillinger-Weber potentials for Si and Ge. *Phys. Rev. B* **1990**, *41*, 12915–12918. [CrossRef]
51. Dodson, B.W. Development of a many-body Tersoff-type potential for silicon. *Phys. Rev. B* **1987**, *35*, 2795–2798. [CrossRef]
52. Becquart, C.S.; Decker, K.M.; Domain, C.; Ruste, J.; Souffez, Y.; Turbatte, J.C.; Duysen, J.C.V. Massively parallel molecular dynamics simulations with EAM potentials. *Radiat. Eff. Defects Solids* **1997**, *142*, 9–21. [CrossRef]
53. Xu, W.; Kim, W.K. Molecular dynamics simulation of the uniaxial tensile test of silicon nanowires using the MEAM potential. *Mech. Mater.* **2019**, *137*, 103140. [CrossRef]
54. Lee, E.; Lee, K.R.; Baskes, M.I.; Lee, B.J. A modified embedded-atom method interatomic potential for ionic systems. *Phys. Rev. B* **2016**, *93*, 144110. [CrossRef]
55. Toghraie Semironi, D.; Azimian, A.R. Molecular dynamics simulation of liquid–vapor phase equilibrium by using the modified Lennard-Jones potential function. *Heat Mass Transf.* **2010**, *46*, 287–294. [CrossRef]
56. Alejandre, J.; Tildesley, D.J.; Chapela, G.A. Molecular dynamics simulation of the orthobaric densities and surface tension of water. *J. Chem. Phys.* **1995**, *102*, 4574–4583. [CrossRef]
57. Panagiotopoulos, A.Z. Direct Determination of Fluid Phase Equilibria by Simulation in the Gibbs Ensemble: A Review. *Mol. Simul.* **1992**, *9*, 1–23. [CrossRef]
58. Chen, F.; Smith, P.E. Simulated surface tensions of common water models. *J. Chem. Phys.* **2007**, *126*, 221101. [CrossRef]
59. Zakharov, V.V.; Brodskaya, E.N.; Laaksonen, A. Surface tension of water droplets: A molecular dynamics study of model and size dependencies. *J. Chem. Phys.* **1997**, *107*, 10675–10683. [CrossRef]

60. Schaefer, D.; Stephan, S.; Langenbach, K.; Horsch, M.T.; Hasse, H. Mass Transfer through Vapor–Liquid Interfaces Studied by Non-Stationary Molecular Dynamics Simulations. *J. Phys. Chem. B* **2023**, *127*, 2521–2533. [CrossRef]
61. Bernagozzi, M.; Georgoulas, A.; Miché, N.; Marengo, M. Heat pipes in battery thermal management systems for electric vehicles: A critical review. *Appl. Therm. Eng.* **2023**, *219*, 119495. [CrossRef]
62. Long, L.N.; Micci, M.M.; Wong, B.C. Molecular dynamics simulations of droplet evaporation. *Comput. Phys. Commun.* **1996**, *96*, 167–172. [CrossRef]
63. Walther, J.H.; Koumoutsakos, P. Molecular Dynamics Simulation of Nanodroplet Evaporation. *J. Heat Transf.* **2001**, *123*, 741–748. [CrossRef]
64. Yang, T.H.; Pan, C. Molecular dynamics simulation of a thin water layer evaporation and evaporation coefficient. *Int. J. Heat Mass Transf.* **2005**, *48*, 3516–3526. [CrossRef]
65. Persad, A.H.; Ward, C.A. Expressions for the Evaporation and Condensation Coefficients in the Hertz-Knudsen Relation. *Chem. Rev.* **2016**, *116*, 7727–7767. [CrossRef] [PubMed]
66. Heinen, M.; Vrabec, J. Evaporation sampled by stationary molecular dynamics simulation. *J. Chem. Phys.* **2019**, *151*, 044704. [CrossRef] [PubMed]
67. He, R.; Fu, Y.; He, J.; Yi, P.; Li, T. Analysis of subcritical to supercritical transition of n-heptane/ethanol blends by molecular dynamics simulation. *At. Sprays* **2022**, *32*, 87–106. [CrossRef]
68. Yang, T.; Shen, J.; Zhu, C.; Wu, J. Molecular dynamics investigation on the vapor–liquid interface behavior of long-chain alkanes, alcohols, and their mixtures. *J. Mol. Liq.* **2023**, *375*, 121283. [CrossRef]
69. Daiguji, H. Molecular dynamics study of *n*-alcohols adsorbed on an aqueous electrolyte solution. *J. Chem. Phys.* **2001**, *115*, 1538–1549. [CrossRef]
70. Arcidiacono, S.; Poulikakos, D.; Ventikos, Y. Oscillatory behavior of nanodroplets. *Phys. Rev. E* **2004**, *70*, 011505. [CrossRef] [PubMed]
71. Sheu, W.J.; Liou, N.C. Effect of temporal variation of pressure on vaporization of liquid droplets. *Int. J. Heat Mass Transf.* **1999**, *42*, 4043–4054. [CrossRef]
72. Liu, L.H.; Han, Y.F.; Wang, Q.; Fu, Q.F. Molecular dynamics simulation of droplet evaporation in a one-dimensional standing wave acoustic field. *Int. J. Therm. Sci.* **2023**, *184*, 107939. [CrossRef]
73. Chatterjee, S.; Singh, A.; Chakraborty, M. Molecular Insights into the Effect of Crystal Planes on Droplet Wetting. *Langmuir* **2023**, *39*, 4789–4798. [CrossRef] [PubMed]
74. Dussan, E.B. On the Spreading of Liquids on Solid Surfaces: Static and Dynamic Contact Lines. *Annu. Rev. Fluid Mech.* **1979**, *11*, 371–400. [CrossRef]
75. Koplik, J.; Banavar, J.R. Continuum Deductions from Molecular Hydrodynamics. *Annu. Rev. Fluid Mech.* **1995**, *27*, 257–292. [CrossRef]
76. Chakraborty, M.; Ghosh, U.U.; Chakraborty, S.; DasGupta, S. Thermally enhanced self-propelled droplet motion on gradient surfaces. *RSC Adv.* **2015**, *5*, 45266–45275. [CrossRef]
77. Bertrand, E.; Blake, T.D.; Coninck, J.D. Influence of solid–liquid interactions on dynamic wetting: A molecular dynamics study. *J. Phys. Condens Matter.* **2009**, *21*, 464124. [CrossRef]
78. Blake, T.; De Coninck, J. The influence of solid–liquid interactions on dynamic wetting. *Adv. Colloid Interface Sci.* **2002**, *96*, 21–36. [CrossRef] [PubMed]
79. Blake, T.D. The physics of moving wetting lines. *J. Colloid Interface Sci.* **2006**, *299*, 1–13. [CrossRef]
80. Chakraborty, M.; Chowdhury, A.; Bhusan, R.; DasGupta, S. Molecular Dynamics Study of Thermally Augmented Nanodroplet Motion on Chemical Energy Induced Wettability Gradient Surfaces. *Langmuir* **2015**, *31*, 11260–11268. [CrossRef] [PubMed]
81. Chakraborty, D.; Pathak, S.; Chakraborty, M. Molecular Investigation of Contact Line Movement in Electrowetted Nanodroplets. *Langmuir* **2020**, *36*, 12580–12589. [CrossRef]
82. Pathak, S.; Chakraborty, M.; DasGupta, S. Molecular Investigation of the Actuation of Electrowetted Nanodroplets. *Langmuir* **2022**, *38*, 3656–3665. [CrossRef] [PubMed]
83. Walther, J.H.; Jaffe, R.L.; Kotsalis, E.M.; Werder, T.; Halicioglu, T.; Koumoutsakos, P. Hydrophobic hydration of C60 and carbon nanotubes in water. *Carbon* **2004**, *42*, 1185–1194. [CrossRef]
84. Werder, T.; Walther, J.H.; Jaffe, R.L.; Halicioglu, T.; Koumoutsakos, P. On the Water–Carbon Interaction for Use in Molecular Dynamics Simulations of Graphite and Carbon Nanotubes. *J. Phys. Chem. B* **2008**, *112*, 14090. [CrossRef]
85. Walther, J.H.; Jaffe, R.; Halicioglu, T.; Koumoutsakos, P. Carbon Nanotubes in Water: Structural Characteristics and Energetics. *J. Phys. Chem. B* **2001**, *105*, 9980–9987. [CrossRef]
86. Casto, A.; Bellussi, F.M.; Diego, M.; Fatti, N.D.; Banfi, F.; Maioli, P.; Fasano, M. Water filling in carbon nanotubes with different wettability and implications on nanotube/water heat transfer via atomistic simulations. *Int. J. Heat Mass Transf.* **2023**, *205*, 123868. [CrossRef]
87. Jabbari, F.; Rajabpour, A.; Saedodin, S.; Wongwises, S. Effect of water/carbon interaction strength on interfacial thermal resistance and the surrounding molecular nanolayer of CNT and graphene flake. *J. Mol. Liq.* **2019**, *282*, 197–204. [CrossRef]
88. Du, Y.; Zhou, T.; Zhao, C.; Ding, Y. Molecular dynamics simulation on thermal enhancement for carbon nano tubes (CNTs) based phase change materials (PCMs). *Int. J. Heat Mass Transf.* **2022**, *182*, 122017. [CrossRef]
89. Gurtin, M.E.; Ian Murdoch, A. Surface stress in solids. *Int. J. Solids Struct.* **1978**, *14*, 431–440. [CrossRef]

90. Murdoch, A.I. The propagation of surface waves in bodies with material boundaries. *J. Mech. Phys. Solids* **1976**, *24*, 137–146. [CrossRef]
91. Kiani, K. Nonlocal free dynamic analysis of periodic arrays of single-walled carbon nanotubes in the presence of longitudinal thermal and magnetic fields. *Comput. Math. Appl.* **2018**, *75*, 3849–3872. [CrossRef]
92. Kiani, K. Thermo-mechanical analysis of functionally graded plate-like nanorotors: A surface elasticity model. *Int. J. Mech. Sci.* **2016**, *106*, 39–49. [CrossRef]
93. Kiani, K. Stress analysis of thermally affected rotating nanoshafts with varying material properties. *Acta Mech. Sin.* **2016**, *32*, 813–827. [CrossRef]
94. Zenkour, A.M. Nonlocal transient thermal analysis of a single-layered graphene sheet embedded in viscoelastic medium. *Phys. E Low-Dimens. Syst. Nanostruct.* **2016**, *79*, 87–97. [CrossRef]
95. Semmah, A.; Beg, O.A.; Mahmoud, S.R.; Heireche, H.; Tounsi, A. Thermal buckling properties of zigzag single-walled carbon nanotubes using a refined nonlocal model. *Adv. Mater. Res.* **2014**, *3*, 77–89. [CrossRef]
96. Zare Pakzad, S.; Nasr Esfahani, M.; Tasdemir, Z.; Wollschläger, N.; Li, T.; Li, X.; Yilmaz, M.; Leblebici, Y.; Alaca, B.E. Nanomechanical Modeling of the Bending Response of Silicon Nanowires. *ACS Appl. Nano Mater.* **2023**, *6*, 15465–15478. [CrossRef]
97. Chen, T.; Chiu, M.S.; Weng, C.N. Derivation of the generalized Young-Laplace equation of curved interfaces in nanoscaled solids. *J. Appl. Phys.* **2006**, *100*, 074308. [CrossRef]
98. Zare Pakzad, S.; Nasr Esfahani, M.; Tasdemir, Z.; Wollschlaeger, N.; Li, X.; Li, T.; Yilmaz, M.; Leblebici, Y.; Alaca, B.E. A new characterization approach to study the mechanical behavior of silicon nanowires. *MRS Adv.* **2021**, *6*, 500–505. [CrossRef]
99. Tasdemir, Z.; Peric, O.; Sacchetto, D.; Fantner, G.E.; Leblebici, Y.; Alaca, B.E. Monolithic Fabrication of Silicon Nanowires Bridging Thick Silicon Structures. *IEEE Trans. Nanotechnol.* **2018**, *17*, 1299–1302. [CrossRef]
100. He, J.; Lilley, C.M. Surface Effect on the Elastic Behavior of Static Bending Nanowires. *Nano Lett.* **2008**, *8*, 1798–1802. [CrossRef]
101. Nasr Esfahani, M.; Zare Pakzad, S.; Li, T.; Li, X.; Tasdemir, Z.; Wollschläger, N.; Leblebici, Y.; Alaca, B.E. Effect of Native Oxide on Stress in Silicon Nanowires: Implications for Nanoelectromechanical Systems. *ACS Appl. Nano Mater.* **2022**, *5*, 13276–13285. [CrossRef]
102. Sun, K.; Shi, J.; Ma, L. Atomistic Insights into the Effects of Residual Stress during Nanoindentation. *Crystals* **2017**, *7*, 240. [CrossRef]
103. Kinjo, T.; Matsumoto, M. Cavitation processes and negative pressure. *Fluid Phase Equilib* **1998**, *144*, 343–350. [CrossRef]
104. Kimura, T.; Maruyama, S. Molecular dynamics simulation of heterogeneous nucleation of a liquid droplet on a solid surface. *Microscale Thermophys Eng.* **2002**, *6*, 3–13. [CrossRef]
105. Nagayama, G.; Tsuruta, T.; Cheng, P. Molecular dynamics simulation on bubble formation in a nanochannel. *Int. J. Heat Mass Transf.* **2006**, *49*, 4437–4443. [CrossRef]
106. She, X.; Shedd, T.A.; Lindeman, B.; Yin, Y.; Zhang, X. Bubble formation on solid surface with a cavity based on molecular dynamics simulation. *Int. J. Heat Mass Transf.* **2016**, *95*, 278–287. [CrossRef]
107. Moseler, M.; Landman, U. Formation, Stability, and Breakup of Nanojets. *Science* **2000**, *289*, 1165–1169. [CrossRef] [PubMed]
108. Roy, S. Coalescence preference and droplet size inequality during fluid phase segregation. *EPL Europhys. Lett.* **2018**, *121*, 34001. [CrossRef]
109. Yi, N.; Huang, B.; Dong, L.; Quan, X.; Hong, F.; Tao, P.; Song, C.; Shang, W.; Deng, T. Temperature-Induced Coalescence of Colliding Binary Droplets on Superhydrophobic Surface. *Sci. Rep.* **2014**, *4*, 4303. [CrossRef]
110. Li, T.; Li, M.; Zhang, L.; Yan, M.; Li, H. Molecular Dynamics Study of the Temperature-Dependent Coalescence of Liquid Nanodrops: Implications for Microfluidics. *ACS Appl. Nano Mater.* **2019**, *2*, 7978–7988. [CrossRef]
111. Song, F.; Niu, H.; Fan, J.; Chen, Q.; Wang, G.; Liu, L. Molecular dynamics study on the coalescence and break-up behaviors of ionic droplets under DC electric field. *J. Mol. Liq.* **2020**, *312*, 113195. [CrossRef]
112. Han, H. *Multiscale Modeling of Nanostructure-Enhanced Two-Phase Heat Transfer*; Drexel University: Philadelphia, PA, USA, 2016.
113. Hu, H.; Sun, Y. Molecular dynamics simulations of disjoining pressure effect in ultra-thin water film on a metal surface. *Appl. Phys. Lett.* **2013**, *103*, 263110. [CrossRef]
114. Hu, H.; Sun, Y. Effect of nanopatterns on Kapitza resistance at a water-gold interface during boiling: A molecular dynamics study. *J. Appl. Phys.* **2012**, *112*, 053508. [CrossRef]
115. Dai, D.; Li, Y.; Wang, Y.; Bao, H.; Wang, G. Rethinking the image feature biases exhibited by deep convolutional neural network models in image recognition. *CAAI Trans. Intell. Technol.* **2022**, *7*, 721–731. [CrossRef]
116. Tunyasuvunakool, K.; Adler, J.; Wu, Z.; Green, T.; Zielinski, M.; Žídek, A.; Bridgland, A.; Cowie, A.; Meyer, C.; Laydon, A. Highly accurate protein structure prediction for the human proteome. *Nature* **2021**, *596*, 590–596. [CrossRef] [PubMed]
117. Meskhidze, H. Can Machine Learning Provide Understanding? How Cosmologists Use Machine Learning to Understand Observations of the Universe. *Erkenntnis* **2023**, *88*, 1895–1909. [CrossRef] [PubMed]
118. Mallikarjuna, S.B.; Shivakumara, P.; Khare, V.; Basavanna, M.; Pal, U.; Poornima, B. Multi-gradient-direction based deep learning model for arecanut disease identification. *CAAI Trans. Intell. Technol.* **2022**, *7*, 156–166. [CrossRef]
119. Chugo, D.; Muramatsu, S.; Yokota, S.; She, J.H.; Hashimoto, H. Stand-Up Assistive Devices Allowing Patients to Perform Voluntary Movements Within the Safety Movement Tolerance. *J. Artif. Intell. Technol.* **2022**, *2*, 164–173. [CrossRef]
120. Senn, H.M.; Thiel, W. QM/MM Methods for Biomolecular Systems. *Angew. Chem. Int. Ed.* **2009**, *48*, 1198–1229. [CrossRef]

121. Kulik, H.J.; Zhang, J.; Klinman, J.P.; Martínez, T.J. How Large Should the QM Region Be in QM/MM Calculations? The Case of Catechol *O* -Methyltransferase. *J. Phys. Chem. B* **2016**, *120*, 11381–11394. [CrossRef] [PubMed]
122. Wan, X.; Feng, W.; Wang, Y.; Wang, H.; Zhang, X.; Deng, C.; Yang, N. Materials Discovery and Properties Prediction in Thermal Transport via Materials Informatics: A Mini Review. *Nano Lett.* **2019**, *19*, 3387–3395. [CrossRef] [PubMed]
123. Wei, H.; Bao, H.; Ruan, X. Perspective: Predicting and optimizing thermal transport properties with machine learning methods. *Energy AI* **2022**, *8*, 100153. [CrossRef]
124. Khodakarami, S.; Fazle Rabbi, K.; Suh, Y.; Won, Y.; Miljkovic, N. Machine learning enabled condensation heat transfer measurement. *Int. J. Heat Mass Transf.* **2022**, *194*, 123016. [CrossRef]
125. Rustam, S.; Schram, M.; Lu, Z.; Chaka, A.M.; Rosenthal, W.S.; Pfaendtner, J. Optimization of Thermal Conductance at Interfaces Using Machine Learning Algorithms. *ACS Appl. Mater. Interfaces* **2022**, *14*, 32590–32597. [CrossRef]
126. Ma, A.; Dinner, A.R. Automatic Method for Identifying Reaction Coordinates in Complex Systems. *J. Phys. Chem. B* **2005**, *109*, 6769–6779. [CrossRef] [PubMed]
127. Rasmussen, T.D.; Ren, P.; Ponder, J.W.; Jensen, F. Force field modeling of conformational energies: Importance of multipole moments and intramolecular polarization. *Int. J. Quantum. Chem.* **2007**, *107*, 1390–1395. [CrossRef]
128. Dirac, P.A.M. Quantum mechanics of many-electron systems. *Proc. R. Soc. Lond. Ser. A Contain. Pap. A Math. Phys. Character* **1929**, *123*, 714–733. [CrossRef]
129. Karplus, M.; McCammon, J.A. Molecular dynamics simulations of biomolecules. *Nat. Struct. Biol.* **2002**, *9*, 646–652. [CrossRef]
130. Vitalini, F.; Mey, A.S.J.S.; Noé, F.; Keller, B.G. Dynamic properties of force fields. *J. Chem. Phys.* **2015**, *142*, 084101. [CrossRef] [PubMed]
131. Hansen, K.; Montavon, G.; Biegler, F.; Fazli, S.; Rupp, M.; Scheffler, M.; von Lilienfeld, O.A.; Tkatchenko, A.; Müller, K.R. Assessment and Validation of Machine Learning Methods for Predicting Molecular Atomization Energies. *J. Chem. Theory Comput.* **2013**, *9*, 3404–3419. [CrossRef] [PubMed]
132. Unke, O.T.; Chmiela, S.; Sauceda, H.E.; Gastegger, M.; Poltavsky, I.; Schütt, K.T.; Tkatchenko, A.; Müller, K.M. Machine Learning Force Fields. *Chem. Rev.* **2021**, *121*, 10142–10186. [CrossRef]
133. Hansen, K.; Biegler, F.; Ramakrishnan, R.; Pronobis, W.; von Lilienfeld, O.A.; Müller, K.R.; Tkatchenko, A. Machine Learning Predictions of Molecular Properties: Accurate Many-Body Potentials and Nonlocality in Chemical Space. *J. Phys. Chem. Lett.* **2015**, *6*, 2326–2331. [CrossRef] [PubMed]
134. Kadupitiya, J.C.; Sun, F.; Fox, G.; Jadhao, V. Machine learning surrogates for molecular dynamics simulations of soft materials. *J. Comput. Sci.* **2020**, *42*, 101107. [CrossRef]
135. Wang, Y.; Lamim Ribeiro, J.M.; Tiwary, P. Machine learning approaches for analyzing and enhancing molecular dynamics simulations. *Curr. Opin. Struct. Biol.* **2020**, *61*, 139–145. [CrossRef]
136. Behler, J.; Parrinello, M. Generalized Neural-Network Representation of High-Dimensional Potential-Energy Surfaces. *Phys. Rev. Lett.* **2007**, *98*, 146401. [CrossRef] [PubMed]
137. Bartók, A.P.; Payne, M.C.; Kondor, R.; Csányi, G. Gaussian Approximation Potentials: The Accuracy of Quantum Mechanics, without the Electrons. *Phys. Rev. Lett.* **2010**, *104*, 136403. [CrossRef] [PubMed]
138. Smith, J.S.; Isayev, O.; Roitberg, A.E. ANI-1, an extensible neural network potential with DFT accuracy at force field computational cost. *Chem. Sci.* **2017**, *8*, 3192–3203. [CrossRef]
139. Bao, H.; Chen, J.; Gu, X.; Cao, B. A Review of Simulation Methods in Micro/Nanoscale Heat Conduction. *ES Energy Environ.* **2018**, *1*, 16–55. [CrossRef]
140. Wang, Y.; Vallabhaneni, A.K.; Qiu, B.; Ruan, X. Two-Dimensional Thermal Transport in Graphene: A Review of Numerical Modeling Studies. *Nanoscale Microscale Thermophys Eng.* **2014**, *18*, 155–182. [CrossRef]
141. Saito, R.; Mizuno, M.; Dresselhaus, M.S. Ballistic and Diffusive Thermal Conductivity of Graphene. *Phys. Rev. Appl.* **2018**, *9*, 024017. [CrossRef]
142. Li, H.-P.; Zhang, R.-Q. Anomalous effect of hydrogenation on phonon thermal conductivity in thin silicon nanowires. *EPL Europhys. Lett.* **2014**, *105*, 56003. [CrossRef]
143. Tian, Z.; Hu, H.; Sun, Y. A molecular dynamics study of effective thermal conductivity in nanocomposites. *Int. J. Heat Mass Transf.* **2013**, *61*, 577–582. [CrossRef]
144. Guo, Y.; Wang, M. Phonon hydrodynamics and its applications in nanoscale heat transport. *Phys. Rep.* **2015**, *595*, 1–44. [CrossRef]
145. Chen, G.; Yang, R.; Chen, X. Nanoscale heat transfer and thermal-electric energy conversion. *J. Phys. IV* **2005**, *125*, 499–504. [CrossRef]
146. Silva, A.C.A.; Neto, E.S.F.; da Silva, S.W.; Morais, P.C.; Dantas, N.O. Modified Phonon Confinement Model and Its Application to CdSe/CdS Core–Shell Magic-Sized Quantum Dots Synthesized in Aqueous Solution by a New Route. *J. Phys. Chem. C* **2013**, *117*, 1904–1914. [CrossRef]
147. Song, Q.; Chen, G. Evaluation of the diffuse mismatch model for phonon scattering at disordered interfaces. *Phys. Rev. B* **2021**, *104*, 085310. [CrossRef]
148. Lindsay, L.; Broido, D.A.; Mingo, N. Lattice thermal conductivity of single-walled carbon nanotubes: Beyond the relaxation time approximation and phonon-phonon scattering selection rules. *Phys. Rev. B-Condens. Matter. Mater. Phys.* **2009**, *80*, 125407. [CrossRef]

149. Mingo, N.; Broido, D.A. Length dependence of carbon nanotube thermal conductivity and the "problem of long waves". *Nano Lett.* **2005**, *5*, 1221–1225. [CrossRef] [PubMed]
150. Zhang, Z.; Ouyang, Y.; Cheng, Y.; Chen, J.; Li, N. Size-dependent phononic thermal transport in low-dimensional nanomaterials. *Phys. Rep.* **2020**, *860*, 1–26. [CrossRef]
151. Polanco, J.; Fitzgerald, R.M.; Maradudin, A.A. Scattering of surface plasmon polaritons by one-dimensional surface defects. *Phys. Rev. B-Condens. Matter. Mater. Phys.* **2013**, *87*, 155417. [CrossRef]
152. Xiong, S.; Kosevich, Y.A.; Sääskilahti, K.; Ni, Y.; Volz, S. Tunable thermal conductivity in silicon twinning superlattice nanowires. *Phys. Rev. B-Condens. Matter. Mater. Phys.* **2014**, *90*, 195439. [CrossRef]
153. Xiong, S.; Sääskilahti, K.; Kosevich, Y.A.; Han, H.; Donadio, D.; Volz, S. Blocking Phonon Transport by Structural Resonances in Alloy-Based Nanophononic Metamaterials Leads to Ultralow Thermal Conductivity. *Phys. Rev. Lett.* **2016**, *117*, 025503. [CrossRef] [PubMed]
154. Maire, J.; Anufriev, R.; Nomura, M. Ballistic thermal transport in silicon nanowires. *Sci. Rep.* **2017**, *7*, 41794. [CrossRef] [PubMed]
155. Raja, S.N.; Rhyner, R.; Vuttivorakulchai, K.; Luisier, M.; Poulikakos, D. Length scale of diffusive phonon transport in suspended thin silicon nanowires. *Nano Lett.* **2017**, *17*, 276–283. [CrossRef]
156. Schelling, P.K.; Phillpot, S.R.; Keblinski, P. Comparison of atomic-level simulation methods for computing thermal conductivity. *Phys. Rev. B-Condens. Matter. Mater. Phys.* **2002**, *65*, 144306. [CrossRef]
157. Sellan, D.P.; Landry, E.S.; Turney, J.E.; McGaughey, A.J.H.; Amon, C.H. Size effects in molecular dynamics thermal conductivity predictions. *Phys. Rev. B-Condens. Matter. Mater. Phys.* **2010**, *81*, 214305. [CrossRef]
158. Ye, Z.Q.; Cao, B.Y. Spectral phonon thermal properties in graphene nanoribbons. *Carbon* **2015**, *93*, 915–923. [CrossRef]
159. Squires, T.M.; Quake, S.R. Microfluidics: Fluid physics at the nanoliter scale. *Rev. Mod. Phys.* **2005**, *77*, 977–1026. [CrossRef]
160. Whitesides, G.M. The origins and the future of microfluidics. *Nature* **2006**, *442*, 368–373. [CrossRef]
161. Bhagat, A.A.S.; Bow, H.; Hou, H.W.; Tan, S.J.; Han, J.; Lim, C.T. Microfluidics for cell separation. *Med. Biol. Eng. Comput.* **2010**, *48*, 999–1014. [CrossRef]
162. Chaudhury, M.K.; Whitesides, G.M. How to make water run uphill. *Science* **1992**, *256*, 1539–1541. [CrossRef]
163. Im, Y.; Dietz, C.; Lee, S.S.; Joshi, Y. Flower-like CuO nanostructures for enhanced boiling. *Nanoscale Microscale Thermophys Eng.* **2012**, *16*, 145–153. [CrossRef]
164. Chen, X.; Cao, G.; Han, A.; Punyamurtula, V.K.; Liu, L.; Culligan, P.J.; Kim, T.; Qiao, Y. Nanoscale fluid transport: Size and rate effects. *Nano Lett.* **2008**, *8*, 2988–2992. [CrossRef]
165. Abbas, W.; Magdy, M.M. Heat and Mass Transfer Analysis of Nanofluid Flow Based on Cu, Al_2O_3, and TiO_2 over a Moving Rotating Plate and Impact of Various Nanoparticle Shapes. *Math. Probl. Eng.* **2020**, *2020*, 9606382. [CrossRef]
166. Yang, R. Nanoscale Heat Conduction with Applications in Nanoelectronics and Thermoelectrics. Ph.D. Thesis, Massachusetts Institute of Technology, Cambridge, MA, USA, 2005; 217p.
167. Kaneez, H.; Qureshi, M.A.; Alharbi, S.O.; Aziz, T.; Nawaz, M. Role of hybrid nano-structures and dust particles on transportation of heat energy in fluid with memory effects. *Ain. Shams Eng. J.* **2021**, *12*, 2171–2180. [CrossRef]
168. Sivashanmugam, P. Application of Nanofluids in Heat Transfer. In *An Overview of Heat Transfer Phenomena*; InTech: Rijeka, Croatia, 2012; pp. 411–440. [CrossRef]
169. Das, S.K.; Choi, S.U.S.; Patel, H.E. Heat transfer in nanofluids—A review. *Heat Transf. Eng.* **2006**, *27*, 3–19. [CrossRef]
170. Rashid, U.; Lu, D.; Iqbal, Q. Nanoparticles impacts on natural convection nanofluid flow and heat transfer inside a square cavity with fixed a circular obstacle. *Case Stud. Therm. Eng.* **2023**, *44*, 102829. [CrossRef]
171. Ajeeb, W.; Murshed, S.M.S. Nanofluids in compact heat exchangers for thermal applications: A State-of-the-art review. *Therm. Sci. Eng. Prog.* **2022**, *30*, 101276. [CrossRef]
172. Sobhan, C.B.; Peterson, G.P. *Microscale and Nanoscale Heat Transfer Fundamentals and Engineering Applications*, 1st ed.; Peterson, G.P., Ed.; CRC Press: Boca Raton, FL, USA, 2008.
173. Li, X.; Yuan, F.; Tian, W.; Dai, C.; Yang, X.; Wang, D.; Du, J.; Yu, W.; Yuan, H. Heat Transfer Enhancement of Nanofluids with Non-Spherical Nanoparticles: A Review. *Appl. Sci.* **2022**, *12*, 4767. [CrossRef]
174. Maitra, T.; Zhang, S.; Tiwari, M.K. *Thermal Transport in Micro- and Nanoscale Systems*; Springer: Berlin/Heidelberg, Germany, 2018. [CrossRef]
175. Chen, G. Non-Fourier phonon heat conduction at the microscale and nanoscale. *Nat. Rev. Phys.* **2021**, *3*, 555–569. [CrossRef]
176. Gupta, R.; Bera, C. Effect of nanoinclusions on the lattice thermal conductivity of SnSe. *Nano Express* **2020**, *1*, 030035. [CrossRef]
177. Zhang, H.; Qing, S.; Gui, Q.; Zhang, X.; Zhang, A. Effects of surface modification and surfactants on stability and thermophysical properties of TiO_2/water nanofluids. *J. Mol. Liq.* **2022**, *349*, 118098. [CrossRef]
178. Cheng, H.; Zhang, P.; Zhang, Q.; Wu, J.; Dai, Y.; Hu, W.; Wereley, N.M. Effects of surface modification on the stability of suspension and thermal conductivity enhancement of composite fe nanofluids. *IEEE Trans. Magn.* **2014**, *50*, 1–4. [CrossRef]
179. Beck, J.; Palmer, M.; Inman, K.; Wohld, J.; Cummings, M.; Fulmer, R.; Scherer, B.; Vafaei, S. Heat Transfer Enhancement in the Microscale: Optimization of Fluid Flow. *Nanomaterials* **2022**, *12*, 3628. [CrossRef] [PubMed]
180. Nguyen, D.H.; Ahn, H.S. A comprehensive review on micro/nanoscale surface modification techniques for heat transfer enhancement in heat exchanger. *Int. J. Heat Mass Transf.* **2021**, *178*, 121601. [CrossRef]
181. Souayeh, B.; Bhattacharyya, S. Turbulent Heat Transfer Augmentation in a Square Channel by Augmenting the Flow Pattern with Novel Arc-Shaped Ribs. *Mathematics* **2023**, *11*, 1490. [CrossRef]

182. Ghadimi, A.; Saidur, R.; Metselaar, H.S.C. A review of nanofluid stability properties and characterization in stationary conditions. *Int. J. Heat Mass Transf.* **2011**, *54*, 4051–4068. [CrossRef]
183. Yarmand, H.; Gharehkhani, S.; Shirazi, S.F.S.; Goodarzi, M.; Amiri, A.; Sarsam, W.S.; Alehashem, M.S.; Dahari, M.; Kazi, S.N. Study of synthesis, stability and thermo-physical properties of graphene nanoplatelet/platinum hybrid nanofluid. *Int. Commun. Heat Mass Transf.* **2016**, *77*, 15–21. [CrossRef]
184. Goswami, A.; Pillai, S.C.; McGranaghan, G. Micro/Nanoscale surface modifications to combat heat exchanger fouling. *Chem. Eng. J. Adv.* **2023**, *16*, 100519. [CrossRef]
185. Hsu, H.Y.; Lin, M.C.; Popovic, B.; Lin, C.R.; Patankar, N.A. A numerical investigation of the effect of surface wettability on the boiling curve. *PLoS ONE* **2017**, *12*, e0187175. [CrossRef]
186. Heidarshenas, A.; Azizi, Z.; Peyghambarzadeh, S.M.; Sayyahi, S. Experimental investigation of heat transfer enhancement using ionic liquid-Al_2O_3 hybrid nanofluid in a cylindrical microchannel heat sink. *Appl. Therm. Eng.* **2021**, *191*, 116879. [CrossRef]
187. Shahmardi, A.; Tammisola, O.; Chinappi, M.; Brandt, L. Effects of surface nanostructure and wettability on pool boiling: A molecular dynamics study. *Int. J. Therm. Sci.* **2021**, *167*, 106980. [CrossRef]
188. Lee, J.Y.; Kim, M.H.; Kaviany, M.; Son, S.Y. Bubble nucleation in microchannel flow boiling using single artificial cavity. *Int. J. Heat Mass Transf.* **2011**, *54*, 5139–5148. [CrossRef]
189. Chakraborty, P.; Ma, T.; Cao, L.; Wang, Y. Significantly enhanced convective heat transfer through surface modification in nanochannels. *Int. J. Heat Mass Transf.* **2019**, *136*, 702–708. [CrossRef]
190. Besagni, G.; Inzoli, F.; Ziegenhein, T. Two-phase bubble columns: A comprehensive review. *ChemEngineering* **2018**, *2*, 13. [CrossRef]
191. Chen, J.; Ahmad, S.; Cai, J.; Liu, H.; Lau, K.T.; Zhao, J. Latest progress on nanotechnology aided boiling heat transfer enhancement: A review. *Energy* **2021**, *215*, 119114. [CrossRef]
192. Lu, Y.W.; Kandlikar, S.G. Nanoscale surface modification techniques for pool boiling enhancementa—A critical review and future directions. *Heat Transf. Eng.* **2011**, *32*, 827–842. [CrossRef]
193. Yuan, D.; Chen, D.; Yan, X.; Xu, J.; Lu, Q.; Huang, Y. Bubble behavior and its contribution to heat transfer of subcooled flow boiling in a vertical rectangular channel. *Ann. Nucl. Energy* **2018**, *119*, 191–202. [CrossRef]
194. Kancheva, M.; Aronson, L.; Pattilachan, T.; Sautto, F.; Daines, B.; Thommes, D.; Shar, A.; Razavi, M. Bubble-Based Drug Delivery Systems: Next-Generation Diagnosis to Therapy. *J. Funct. Biomater.* **2023**, *14*, 373. [CrossRef]
195. Peng, Z.; Wang, G.; Moghtaderi, B.; Doroodchi, E. A review of microreactors based on slurry Taylor (segmented) flow. *Chem. Eng. Sci.* **2022**, *247*, 117040. [CrossRef]
196. Shahid, M.; Ahmed, W.; Zhan, Y.; Hongtao, Z.; Kaewsaneha, C.; Opaprakasit, P. *Nanosolar Cell Technologies*; Elsevier: Amsterdam, The Netherlands, 2023. [CrossRef]
197. Allen, J.J.; Smits, A.J. Energy Harvesting eel. *J. Fluids Struct.* **2001**, *15*, 629–640. [CrossRef]
198. Biswas, P.K.; Uddin, M.; Islam, M.U.; Sarkar, M.I.; DeSa, V.; Khan, M.; Huq, A. Icme09-Am-29 Harnessing Raindrop Energy in Bangladesh. *Int. Conf. Mech. Eng.* **2009**, *2009*, 26–28.
199. Ilyas, M.A.; Swingler, J. Piezoelectric energy harvesting from raindrop impacts. *Energy* **2015**, *90*, 796–806. [CrossRef]
200. Viola, F.; Romano, P.; Miceli, R.; Acciari, G. On the harvest of rainfall energy by means of piezoelectric transducer. In Proceedings of the 2013 International Conference on Renewable Energy Research and Applications, Madrid, Spain, 20–23 October 2013; pp. 1133–1138. [CrossRef]
201. Valentini, L.; Bon, S.B.; Kenny, J. Liquid droplet excitation of freestanding poly(methyl methacrylate)/ graphene oxide films for mechanical energy harvesting. *J. Polym. Sci. Part B Polym. Phys.* **2013**, *51*, 1028–1032. [CrossRef]
202. Lai, Y.C.; Hsiao, Y.C.; Wu, H.M.; Wang, Z.L. Waterproof-Fabric-Based Multifunctional Triboelectric Nanogenerator for Universally Harvesting Energy from Raindrops, Wind, and Human Motions and as Self-Powered Sensors. *Adv. Sci.* **2019**, *6*, 1801883. [CrossRef]
203. Le, A.T.; Ahmadipour, M.; Pung, S.Y. A review on ZnO-based piezoelectric nanogenerators: Synthesis, characterization techniques, performance enhancement and applications. *J. Alloys Compd.* **2020**, *844*, 156172. [CrossRef]
204. Soin, N.; Shah, T.H.; Anand, S.C.; Geng, J.; Pornwannachai, W.; Mandal, P.; Reid, D.; Sharma, S.; Hadimani, R.L.; Bayramol, D.V.; et al. Novel "3-D spacer" all fibre piezoelectric textiles for energy harvesting applications. *Energy Environ. Sci.* **2014**, *7*, 1670–1679. [CrossRef]
205. Kang, L.; An, H.L.; Park, J.Y.; Hong, M.H.; Nahm, S.; Lee, C.G. La-doped p-type ZnO nanowire with enhanced piezoelectric performance for flexible nanogenerators. *Appl. Surf. Sci.* **2019**, *475*, 969–973. [CrossRef]
206. Tinaikar, A. Harvesting Energy from Rainfall. *Int. J Renew. Sustain. Energy* **2013**, *2*, 130. [CrossRef]
207. Adhikari, A.; Sengupta, J. *Nanogenerators: A New Paradigm in Blue Energy Harvesting*; Elsevier: Amsterdam, The Netherlands, 2021. [CrossRef]
208. Snyder, G.J.; Toberer, E.S. Complex TE meterials. *Nat. Mater.* **2008**, *7*, 105–114. [CrossRef] [PubMed]
209. Rowe, D.M. *CRC Handbook of Thermoelectrics*; Rowe, D.M., Ed.; CRC Press: Boca Raton, FL, USA, 2006.
210. Heremans, J.P.; Dresselhaus, M.S.; Bell, L.E.; Morelli, D.T. When thermoelectrics reached the nanoscale. *Nat. Nanotechnol.* **2013**, *8*, 471–473. [CrossRef] [PubMed]
211. Chen, G. *Nanoscale Energy Transport and Conversion: A Parallel Treatment of Electrons, Molecules, Phonons, and Photons*, 1st ed.; Christensen, D., Ed.; Oxford Universty Press: Oxford, UK, 2005.

212. Sui, J.; Li, J.; He, J.; Pei, Y.L.; Berardan, D.; Wu, H.; Dragoe, N.; Cai, W.; Zhao, L.D. Texturation boosts the thermoelectric performance of BiCuSeO oxyselenides. *Energy Environ. Sci.* **2013**, *6*, 2916–2920. [CrossRef]
213. Minnich, A.J.; Dresselhaus, M.S.; Ren, Z.F.; Chen, G. Bulk nanostructured thermoelectric materials: Current research and future prospects. *Energy Environ. Sci.* **2009**, *2*, 466–479. [CrossRef]
214. Shakouri, A. Recent developments in semiconductor thermoelectric physics and materials. *Annu. Rev. Mater. Res.* **2011**, *41*, 399–431. [CrossRef]
215. Venkatasubramanian, R.; Siivola, E.; Colpitts, T.; O'Quinn, B. Thin-film thermoelectric devices with high room-temperature figures of merit. *Nature* **2001**, *413*, 597–602. [CrossRef] [PubMed]
216. He, J.; Kanatzidis, M.G.; Dravid, V.P. High performance bulk thermoelectrics via a panoscopic approach. *Mater. Today* **2013**, *16*, 166–176. [CrossRef]
217. Zhao, L.D.; Lo, S.H.; Zhang, Y.; Sun, H.; Tan, G.; Uher, C.; Wolverton, C.; Dravid, V.P.; Kanatzidis, M.G. Ultralow thermal conductivity and high thermoelectric figure of merit in SnSe crystals. *Nature* **2014**, *508*, 373–377. [CrossRef]
218. Alahmad, M.; El-Aleem, F.A. Heat Transfer Challenges in Semiconductors Processing and the Applications of Heat Pipes for Efficient Heat Removal. *J. King. Saud. Univ.-Eng. Sci.* **2003**, *15*, 141–154. [CrossRef]
219. Simons, R.E.; Antonetti, V.W.; Nakayama, W.; Oktay, S. Heat Transfer in Electronic Packages. In *Microelectronics Packaging Handbook*; Springer: New York, NY, USA, 1997; Volume 6, pp. 314–403. [CrossRef]
220. Gurrum, S.P.; Suman, S.K.; Joshi, Y.K.; Fedorov, A.G. Thermal Issues in Next-Generation Integrated Circuits. *IEEE Trans. Device Mater. Reliab.* **2004**, *4*, 709–714. [CrossRef]
221. Kumar, J.P.S.; Sankaranarayanan, R.; Sujana, J.A.J.; Hynes, N.R.J. Advantages and disadvantages of nanodevices. In *Nanomedicine Manufacturing and Applications*; Elsevier: Amsterdam, The Netherlands, 2021; pp. 163–171. [CrossRef]
222. Espinosa, H.D.; Ke, C.; Pugno, N. Nanoelectromechanical Systems: Experiments and Modeling. In *Encyclopedia of Materials: Science and Technology*; Elsevier: Amsterdam, The Netherlands, 2006; pp. 1–9. [CrossRef]
223. Lei, S.; Su, N.; Li, M. Thermal-Resistance Effect of Graphene at High Temperatures in Nanoelectromechanical Temperature Sensors. *Micromachines* **2022**, *13*, 2078. [CrossRef] [PubMed]
224. Shikida, M.; Hasegawa, Y.; Farisi, M.S.; Al Matsushima, M.; Kawabe, T. Advancements in MEMS technology for medical applications: Microneedles and miniaturized sensors. *JPN J. Appl. Phys.* **2022**, *61*, SA0803. [CrossRef]
225. Nemec, D.; Janota, A.; Hrubos, M.; Simak, V. Intelligent Real-Time MEMS Sensor Fusion and Calibration. *IEEE Sens. J.* **2016**, *16*, 7150–7160. [CrossRef]
226. Li, J. Micro-/Nano-Fiber Sensors and Optical Integration Devices. *Sensors* **2022**, *22*, 7673. [CrossRef]
227. Jiao, P.; Matin Nazar, A.; Egbe, K.J.I.; Barri, K.; Alavi, A.H. Magnetic capsulate triboelectric nanogenerators. *Sci. Rep.* **2022**, *12*, 89. [CrossRef]
228. Macenić, M.; Kurevija, T.; Medved, I. Novel geothermal gradient map of the Croatian part of the Pannonian Basin System based on data interpretation from 154 deep exploration wells. *Renew. Sustain. Energy Rev.* **2020**, *132*, 110069. [CrossRef]
229. Jiang, X.; Kazarin, P.; Sinanis, M.D.; Darwish, A.; Raghunathan, N.; Alexeenko, A.; Peroulis, D. A non-invasive multipoint product temperature measurement for pharmaceutical lyophilization. *Sci. Rep.* **2022**, *12*, 12010. [CrossRef] [PubMed]
230. Takács, G.; Bognár, G.; Bándy, E.; Rózsás, G.; Szabó, P.G. Fabrication and characterization of microscale heat sinks. *Microelectron. Reliab.* **2017**, *79*, 480–487. [CrossRef]
231. Sundén, B.; Fu, J. Heat Pipes for Aerospace Application. In *Heat Transfer in Aerospace Applications*; Elsevier: Amsterdam, The Netherlands, 2017; pp. 117–144. [CrossRef]
232. Reay, D.A.; Kew, P.A.; McGlen, R.J. Cooling of electronic components. In *Heat Pipes*; Elsevier: Amsterdam, The Netherlands, 2014; pp. 207–225. [CrossRef]
233. Jouhara, H. 4.3 Heat Pipes. In *Comprehensive Energy Systems*; Elsevier: Amsterdam, The Netherlands, 2018; pp. 70–97. [CrossRef]
234. Faghri, A.; Zhang, Y. Introduction to transport phenomena. In *Transport Phenomena in Multiphase Systems*; Elsevier: Amsterdam, The Netherlands, 2006; pp. 1–106. [CrossRef]
235. Chen, X.; Shen, S.; Guo, L.; Mao, S.S. Semiconductor-based photocatalytic hydrogen generation. *Chem. Rev.* **2010**, *110*, 6503–6570. [CrossRef] [PubMed]
236. Guo, C.F.; Sun, T.; Cao, F.; Liu, Q.; Ren, Z. Metallic nanostructures for light trapping in energy-harvesting devices. *Light. Sci. Appl.* **2014**, *3*, e161. [CrossRef]
237. Lee, J.; Mubeen, S.; Ji, X.; Stucky, G.D.; Moskovits, M. Plasmonic photoanodes for solar water splitting with visible light. *Nano Lett.* **2012**, *12*, 5014–5019. [CrossRef]
238. Won, D.H.; Shin, H.; Koh, J.; Won, D.H.; Shin, H.; Koh, J.; Chung, J.; Lee, H.S.; Kim, H.; Woo, S.I. Highly Efficient, Selective, and Stable CO_2 Electroreduction on a Hexagonal Zn Catalyst. *Angew. Chem.-Int. Ed.* **2016**, *55*, 9297–9300. [CrossRef]
239. Du, J.; Li, F.; Sun, L. Metal-organic frameworks and their derivatives as electrocatalysts for the oxygen evolution reaction. *Chem. Soc. Rev.* **2021**, *50*, 2663–2695. [CrossRef] [PubMed]
240. Pak, J.; Jang, J.; Cho, K.; Kim, T.Y.; Kim, J.K.; Song, Y.; Hong, W.K.; Min, M.; Lee, H.; Lee, T. Enhancement of photodetection characteristics of MoS2 field effect transistors using surface treatment with copper phthalocyanine. *Nanoscale* **2015**, *7*, 18780–18788. [CrossRef]
241. Hu, H.; Xu, C.; Zhao, Y.; Ziegler, K.J.; Chung, J.N. Boiling and quenching heat transfer advancement by nanoscale surface modification. *Sci. Rep.* **2017**, *7*, 6117. [CrossRef] [PubMed]

242. Das, S.; Bhaumik, S. Enhancement of Nucleate Pool Boiling Heat Transfer on Titanium Oxide Thin Film Surface. *Arab. J. Sci. Eng.* **2014**, *39*, 7385–7395. [CrossRef]
243. Bongarala, M.; Hu, H.; Weibel, J.A.; Garimella, S.V. Microlayer evaporation governs heat transfer enhancement during pool boiling from microstructured surfaces. *Appl. Phys. Lett.* **2022**, *120*, 221602. [CrossRef]
244. Hu, H.; Chakraborty, M.; Allred, T.P.; Weibel, J.A.; Garimella, S.V. Multiscale Modeling of the Three-Dimensional Meniscus Shape of a Wetting Liquid Film on Micro-/Nanostructured Surfaces. *Langmuir* **2017**, *33*, 12028–12037. [CrossRef] [PubMed]
245. Hu, H.; Weibel, J.A.; Garimella, S.V. Role of nanoscale roughness in the heat transfer characteristics of thin film evaporation. *Int. J. Heat Mass Transf.* **2020**, *150*, 119306. [CrossRef]
246. Hasan, M.N.; Shavik, S.M.; Rabbi, K.F.; Mukut, K.M.; Alam, M.M. Thermal transport during thin-film argon evaporation over nanostructured platinum surface: A molecular dynamics study. *Proc. Inst. Mech. Eng. Part N J. Nanomater. Nanoeng. Nanosyst.* **2018**, *232*, 83–91. [CrossRef]
247. Plawsky, J.L.; Fedorov, A.G.; Garimella, S.V.; Ma, H.B.; Maroo, S.C.; Chen, L.; Nam, Y. Nano-and microstructures for thin-film evaporation—A review. *Nanoscale Microscale Thermophys Eng.* **2014**, *18*, 251–269. [CrossRef]
248. Davoodabadi, A.; Ghasemi, H. Evaporation in nano/molecular materials. *Adv. Colloid Interface Sci.* **2021**, *290*, 102385. [CrossRef] [PubMed]
249. Ward, C.A. Liquid-Vapour Phase Change Rates and Interfacial Entropy Production. *J. Non-Equilibrium Thermodyn.* **2002**, *27*, 289–303. [CrossRef]
250. Deng, Y.; Chen, L.; Liu, Q.; Yu, J.; Wang, H. Nanoscale View of Dewetting and Coating on Partially Wetted Solids. *J. Phys. Chem. Lett.* **2016**, *7*, 1763–1768. [CrossRef] [PubMed]
251. Ciraci, S.; Buldum, A.; Batra, I.P. Quantum effects in electrical and thermal transport through nanowires. *J. Phys. Condens Matter.* **2001**, *13*, R537–R568. [CrossRef]
252. Sun, T.; Wang, J.; Kang, W. Van der Waals interaction-tuned heat transfer in nanostructures. *Nanoscale* **2013**, *5*, 128–133. [CrossRef] [PubMed]
253. Laliotis, A.; de Silans, T.P.; Maurin, I.; Ducloy, M.; Bloch, D. Casimir–Polder interactions in the presence of thermally excited surface modes. *Nat. Commun.* **2014**, *5*, 4364. [CrossRef]
254. Xu, L.; Molinero, V. Liquid–Vapor Oscillations of Water Nanoconfined between Hydrophobic Disks: Thermodynamics and Kinetics. *J. Phys. Chem. B* **2010**, *114*, 7320–7328. [CrossRef] [PubMed]
255. Maroo, S.C.; Chung, J.N. Nanoscale liquid-vapor phase-change physics in nonevaporating region at the three-phase contact line. *J. Appl. Phys.* **2009**, *106*, 064911. [CrossRef]
256. Pekur, D.V.; Sorokin, V.M.; Nikolaenko, Y.E. Thermal characteristics of a compact LED luminaire with a cooling system based on heat pipes. *Therm. Sci. Eng. Prog.* **2020**, *18*, 100549. [CrossRef]